České vysoké učení technické v Praze
Fakulta jaderná a fyzikálně inženýrská

Katedra fyziky
Obor: Jaderná a částicová fyzika

Studium fotoprodukce J/ψ na experimentu STAR

VÝZKUMNÝ ÚKOL

Vypracovala: Bc. Michaela Svěráková
Vedoucí práce: doc. Mgr. Jaroslav Bielčík, Ph.D.
Rok: 2023

Czech Technical University in Prague
Faculty of Nuclear Sciences and Physical Engineering

Department of Physics
Field: Nuclear and Particle Physics

Study of J/ψ Photoproduction at the STAR Experiment

RESEARCH PROJECT

Author: Bc. Michaela Svěráková
Supervisor: doc. Mgr. Jaroslav Bielčík, Ph.D.
Year: 2023

FAKULTA JADERNÁ A FYZIKÁLNĚ INŽENÝRSKÁ
KATEDRA FYZIKY

VÝZKUMNÝ ÚKOL

Akademický rok: 2022/2023

Student: Bc. Michaela Svěráková

Studijní program: Jaderná a částicová fyzika

Vedoucí úkolu: doc. Mgr. Jaroslav Bielčík Ph.D.
Ing. Jaroslav Adam, Ph.D. (konzultant)
Ing. Tomáš Truhlář (konzultant)

Název úkolu:
(česky): Studium fotoprodukce J/psi na experimentu STAR

(anglicky): Study of J/psi photoproduction at the STAR experiment

Jazyk VÚ: Angličtina

Pokyny pro vypracování:

1) Difrakční fotoprodukce
2) Nedávné výsledky fotoprodukce J/psi ve srážkách p+p/d
3) Rekonstrukce J/psi v datech z p+p srážek při 510 GeV
4) Diskuze řešení s výhled

Literatura:

[1] V.Barone, E. Predazzi: High Energy Particle Diffraction, Springer (2002)
[2] P.A. Zyla et al. (PDG), Prog. Teor. Exp. Phys. 2020, 083C1 (2021)
[3] S. Acharya et al., Eur. Phys. J. C (2019) 79:402
[4] M. S. Abdallah et al., Phys. Rev. Lett. 128, 122303 (2022)
[5] S.Klein, J. Nystrand, Physics Today 70, 10, 40 (2017)

Datum zadání: 20.10.2022

Datum odevzdání: 15.08.2023

Výzkumný úkol odevzdá student v elektronické podobě nahráním souboru ve formátu pdf do příslušné události v systému Indico. Vedoucí úkolu přiloží své písemné vyjádření k práci studenta s doporučením pro hodnocení.

.....
garant programu

.....
vedoucí katedry

Prohlášení

Prohlašuji, že jsem svůj výzkumný úkol vypracovala samostatně a použila jsem pouze podklady (literaturu, projekty, SW atd.) uvedené v přiloženém seznamu.

Nemám závažný důvod proti použití tohoto školního díla ve smyslu §60 Zákona č. 121/2000 Sb., o právu autorském, o právech souvisejících s právem autorským a o změně některých zákonů (autorský zákon).

V Praze dne ....

Bc. Michaela Svěráková

Acknowledgements

I would like to thank my supervisor doc. Mgr. Jaroslav Bielčík, Ph.D. for his support and guidance through this work. I would also like to thank Włodek Guryn, Ph.D. and William Schmidke Ph.D. for their valuable advice about the analysis method and constructive comments. Furthermore, I want to thank Ing. Tomáš Truhlář and Ing. Jaroslav Adam Ph.D. for their time spend helping with the analysis.

Bc. Michaela Svěráková

Název práce:	**Studium fotoprodukce J/ψ na experimentu STAR**
Autor:	Bc. Michaela Svěráková
Studijní program:	Aplikace přírodních věd
Obor:	Jaderná a částicová fyzika
Druh práce:	Výzkumný úkol
Vedoucí práce:	doc. Mgr. Jaroslav Bielčík, Ph.D., Katedra fyziky, Fakulta jaderná a fyzikálně inženýrská, České vysoké učení technické v Praze
Konzultant:	Ing. Jaroslav Adam, Ph.D., Katedra fyziky, Fakulta jaderná a fyzikálně inženýrská, České vysoké učení technické v Praze Ing. Tomáš Truhlář, Katedra fyziky, Fakulta jaderná a fyzikálně inženýrská, České vysoké učení technické v Praze

Abstrakt: Studium fotoprodukce v ultraperiferních srážkách (UPC) je významným zaměřením v oblasti fyziky vysokých energií. V UPC dvě interagující částice (typicky protony nebo jádra) ze sražených svazků proletí blízko sebe a interagují pouze elektromagnetickou interakcí. Toto je možné popsat jako interakce jedné částice s druhou skrz foton. Zajímavou možností je zkoumání foton-jaderných interakcí, které probíhají difrakčními procesy, ve kterých zůstává druhá částice neporušená. Výzkum fotoprodukce vektorových mezonů, jako je J/ψ v UPC, umožňuje mimo jiné zkoumat partonové distribuční funkce. Hlavními experimenty, na kterých je fotoprodukce zkoumána jsou STAR v BNL a ALICE v CERNu. Cílem této práce je prozkoumat fotoprodukci vektorového mezonu J/ψ v proton-protonových srážkách při energii 510 GeV na experimentu STAR pomocí jeho jedinečné schopnosti měřit dopředné protony pomocí detektorů zvaných Římské nádoby. Podařilo se nám identifikovat J/ψ v rozpadovém kanále na elektron-pozitronové páry. Stanovili jsme kombinatorické pozadí, identifikovali J/ψ mezony v datech a určili jsme surový výtěžek. Pomocí veličiny „chybějící příčná hybnost“, jejíž výpočet vychází ze zákona zachování hybnosti ve srážce, zkoumáme možnost zjistit hodnotu příčné hybnosti virtuálního fotonu přítomného ve fotoprodukci.

Klíčová slova: difrakční proces, fotoprodukce, Římská nádoba, STAR, RHIC

Title:	**Study of J/ψ Photoproduction at the STAR Experiment**
Author:	Bc. Michaela Svěráková
Programme:	Application of Natural Sciences
Field:	Nuclear and Particle Physics
Type of thesis:	Research Project
Supervisor:	doc. Mgr. Jaroslav Bielčík, Ph.D., Department of Physics, Faculty of Nuclear Sciences and Physical Engineering, Czech Technical University in Prague
Consultant:	Ing. Jaroslav Adam, Ph.D., Department of Physics, Faculty of Nuclear Sciences and Physical Engineering, Czech Technical University in Prague Ing. Tomáš Truhlář, Department of Physics, Faculty of Nuclear Sciences and Physical Engineering, Czech Technical University in Prague

Abstract: The study of photoproduction in ultra-peripheral collisions (UPCs) is an important focus in the field of high-energy physics. In UPCs, two interacting particles (typically protons or nuclei) from the colliding beams fly close together and interact only through electromagnetic interaction. This can be described as one particle interacting with the other via a photon. An interesting possibility is the investigation of photon-nuclear interactions that take place through diffractive processes, in which the target nucleus remains intact. Research of photoproduction of vector mesons such as J/ψ in UPCs allows, among other things, to investigate parton distribution functions. The main experiments where photoproduction is investigated are STAR at BNL and ALICE at CERN. The goal of this work is to investigate the photoproduction of J/ψ vector meson in proton-proton collisions at 510 GeV at the STAR experiment using its unique ability to measure forward protons using the Roman Pot detectors. We managed to identify J/ψ through the decay channel to electron-positron pairs. We determined the combinatorial background, identified the J/ψ mesons in the data, and determined the raw yield. Using the quantity of the missing transverse momentum, the calculation of which is based on the law of conservation of momentum in the collision, we investigate the possibility to determine the value of the transverse momentum of the virtual photon present in the photoproduction.

Key words: diffractive process, photoproduction, Roman Pot, STAR, RHIC

Contents

List of Figures

Introduction

This thesis introduces the theory of hadronic diffraction, investigating its theoretical foundations and its connection with classical optics in the context of particle physics. The exploration includes the topics of ultraperipheral collisions and the photoproduction of vector mesons. Recent experimental findings from the ALICE and STAR collaborations are analysed to enhance the understanding of the presented theory. Beyond theoretical aspects, the thesis presents a detailed description of data analysis of proton-proton collisions collected at the STAR experiment, specifically focusing on the photoproduction of J/ψ vector meson.

The first chapter provides an overview of the fundamental theory of hadronic diffraction, drawing parallels with classical optics to illustrate their shared principles. This intriguing connection between optics and hadronic diffraction is shown, spotlighting Kirchhoff's Theory and the Eikonal Approximation as crucial links in the optical to particle physics analogy.

Subsequently, ultraperipheral collisions are explored, which arise when two relativistic nuclei interact electromagnetically without undergoing strong nuclear interactions. The unique insights these collisions offer into the behaviour of hadronic systems under extreme conditions are discussed.

The following investigation of kinematics further deals with the complexities of two-body and single-inclusive processes, and the introduction of Regge Theory offers a valuable framework for understanding hadronic behaviours across various energy scales.

The focus then turns to the photoproduction of vector mesons, involving the creation of these mesons through interactions between high-energy photons and a target nucleus. This process serves as a vital tool for probing quantum chromodynamics (QCD) and nucleon structure.

The second chapter presents recent experimental results from prominent collaborations like ALICE and STAR, providing insights into hadronic diffraction and J/ψ photoproduction. The interpretation of these results provides input for theoretical models and deepens our understanding of the underlying physics.

The third and fourth chapter of the thesis outline my data analysis work that focuses on J/ψ photoproduction in proton-proton collisions and include a discussion of the results. This analysis utilizes the unique ability of the STAR experiment, which is the detection of forward-going protons using the Beam Beam Counter and Roman Pot detectors. The goal of my work is the first look at this data set and measurement of the photoproduction process.

The J/ψ vector meson is identified through its decay into electron-positron pairs. The electron and positron tracks are detected in the Time Projection Chamber and Barrel Electromagnetic Calorimeter. The first step of the analysis is to fine-tune data selection criteria to acquire a clean sample of data for analysis. This is followed by obtaining the uncorrected invariant mass distribution of the electron-positron pairs. The combinatorial background consisting of electron-electron and positron-positron pairs is determined and subtracted in order to calculate the raw yield.

The next step is checking the balance between the forward proton and the reconstructed J/ψ in transverse momenta and azimuthal angle to verify the conservation of momentum in the collision. Following the idea of momentum conservation, we look at the distribution of the transverse momenta missing from the interaction, from which it should be possible to obtain the transverse momentum of the virtual photon present in the interaction.

Chapter 1

Hadronic Diffraction

Information in this chapter is based on literature [1, 2, 3] if not stated otherwise. The wish to understand the internal structure of hadrons and parton distribution functions (PDFs) is a foundational goal in high-energy physics. This effort has driven the development of the Standard Model of particle physics [4], offering a theoretical framework for describing the universe's fundamental constituents and their interactions. The Standard Model incorporates the combination of fermions, the building blocks of matter, and bosons, the force carriers responsible for mediating interactions between particles. Within this model, quarks and gluons have their own roles, with quarks forming the constituents of protons and neutrons, and gluons acting as the carriers of the strong nuclear force that binds quarks together.

To explore these phenomena and probe the subatomic world at unprecedented scales, scientists have built particle accelerators, that are used as microscopes: the Large Hadron Collider (LHC) at CERN, the Relativistic Heavy Ion Collider (RHIC) at Brookhaven National Laboratory and others. The LHC, with its 27-kilometre ring, accelerates protons and heavy ions, colliding them with unmatched energy. This machine has enabled researchers to achieve unprecedented resolutions in the study of subatomic interactions. Similarly, the RHIC focuses on heavy ion collisions to replicate early universe conditions, unveiling the properties of quark-gluon plasma as well as proton-proton collisions that are the topic of this thesis. These accelerators, with their immense capabilities and high resolutions, have revolutionized our understanding of the universe and of particle interactions.

The data produced by these accelerators have led to the validation of the Standard Model's predictions and have paved the way for groundbreaking discoveries, such as the discovery of the Higgs boson at the LHC [5]. As these accelerators continue to push boundaries, the quest for a deeper knowledge of the subatomic world continues. One way to comprehend the structure of hadrons using collision is by studying the interactions in electron collisions, where targets are probed electromagnetically. Another way is to study hadron collisions, which involve strong force interactions carried by gluons. However hadron collisions produce a lot of particles hence are quite messy. Also achieving stronger and stronger accelerators is difficult. So ultra-peripheral collisions (UPCs) are used instead.

Ultraperipheral collisions provide an exciting route to advance our comprehension of particle physics' fundamentals. In these unique events, particles like protons or heavy ions approach each other in collisions with a high impact parameter, meaning that their electromagnetic fields interact, but they do not actually collide. These interactions offer a captivating opportunity to study various phenomena, including photoproduction. The use of UPCs at heavy-ion colliders provides a new tool for probing the gluon density. Studying the kinematics and cross-sections of vector meson photoproduction brings insights into the properties of the target nucleus and the nature of the strong interaction. Exclusive photoproduction of charmonium off a proton is a very clean probe with which to search for saturation effects [6]. This process has been extensively studied in ep interactions at the HERA collider [7]. At high energies, perturbation theory can result in quick growth and dominance of gluon densities at small Bjorken x[1]. Parton saturation is the idea that the occupation numbers of small-x quarks and gluons cannot become arbitrarily large. If left uncontrolled, this growth can result in gluons eternally growing violating a number of mathematical bounds. The resolution to this problem is the phenomena of gluon saturation balancing gluon emissions by recombining gluons at high energies.

1.1 Ultraperipheral Collisions and Diffractive Interaction

This chapter introduces the theory of diffractive interactions with focus on diffractive vector meson photoproduction in proton-proton UPCs as that is the subject of the data analysis part of this work.

Ultraperipheral collisions happen when two accelerated relativistic hadrons "collide" at such high impact parameters that they effectively miss each other. Photon interactions take centre stage as the short-range strong force is reduced. At high energies, protons, Au nuclei, or Pb nuclei which are the most common accelerated hadrons are Lorentz contracted into discs with a width of $1/\gamma$. Since they are moving charged particles, their electric and magnetic fields extend radially outward and surround the ion trajectory, as shown in the diagram in Fig. 1.1. These fields are nearly perpendicular to one another.

One interpretation of relativistic particle fields is through colour dipole model as a flux of nearly real photons. Due to their finite effective mass and lifetime, they are said to be virtual in this context. Nearly real means they have a low mass and long lifetime. Their broad energy spectrum of photons terminates at $\gamma \sim \hbar c/b$, where γ is the Lorentz factor, $\hbar$ is the reduced Planck's constant, c is the speed of light, and b is the impact parameter. The photon flux scales with nuclear charge squared.

The photon can interact with a hadronic target in two distinct ways. The first mode of interaction occurs through electromagnetic coupling to the target, primarily involving charged particles. In the second mode, the photon can undergo oscilla-

[1]Bjorken x is a dimensionless variable, which in photo-proton scattering can be determined by just two variables $x \simeq Q^2/s$. Here $Q^2 = -q^2$ is the photon virtuality and s the centre-of-mass energy

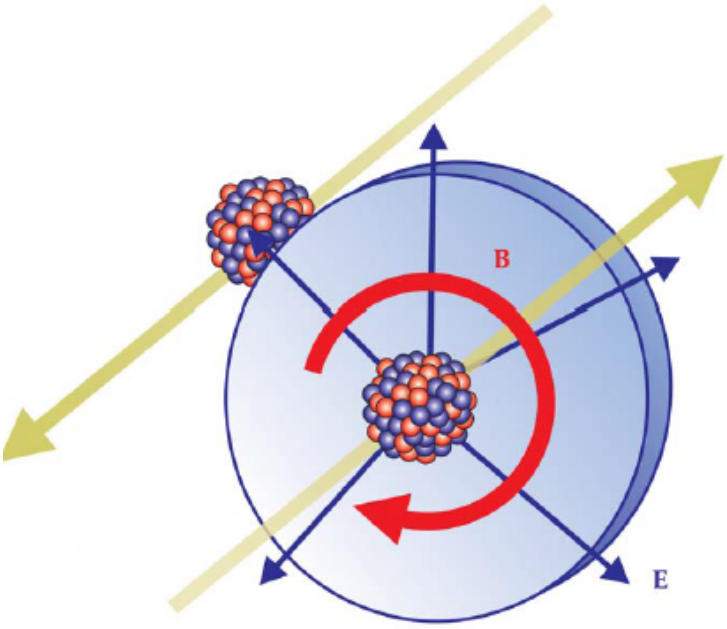

Figure 1.1: Schematic diagram of two colliding nuclei in a ultraperipheral collision. Their original direction is depicted by the yellow arrows. The electric and magnetic fields of one of them is shown in blue and red. Taken from Ref. [3].

tions, effectively transforming into a virtual hadronic state known as a dipole. This dipole state comprises bound quark-antiquark pairs, mesons, or even more complex particles, and it interacts with the target via the strong force. The majority of the photonuclear cross-section is contributed by hadronic fluctuations. The latter are the interactions occurring in vector meson photoproduction.

The single vector meson[2] is created from the interaction of the quark-antiquark pair with the target hadron with a probability given by the overlap integral between the vector meson wave function and the outgoing quark-antiquark pair. As the vector meson is the only produced particle and is measured, we can call this interaction exclusive vector meson photoproduction.

Photon-induced interactions can go two ways. First, there are hadronic processes, which cause the target to disintegrate into tens or hundreds of new particles. Second, there are diffractive interactions, which leave the target intact. The latter are of interest in the context of this thesis.

The following is a general definition of hadronic diffractive processes formulated by Good and Walker in 1960 [8]: a collision at high energy in which no quantum numbers are exchanged between the colliding particles. This indicates that the process proceeds asymptotically whenever the diffused particles and incident particles have the same quantum numbers. This definition represents just a necessary condition for hadronic diffraction, not a sufficient one. Bjorken provided a more practical operational definition in 1994 that is equivalent to the first one [9]: a diffractive reaction is characterized by a large, non-exponentially suppressed, rapidity gap in the final

[2]Vector meson is a meson with total spin 1 and odd parity. This means the spins of the constituent quarks are pointed in the same direction

state. True diffraction, however, can only be distinguished from non-diffraction contributions since the latter decreases exponentially with energy.

Hadronic diffraction was at first included in the soft class of hadronic processes. Meaning the energy scale of the interactions is of the order of nuclear radius R and the transferred momenta in the interaction are small $|t| \sim R^2$. Soft interactions cannot be described successfully by perturbative quantum chromodynamics (pQCD) and Regge theory is used instead. It was later determined that it belongs to a group of interactions that have properties of both soft and hard processes. An example of these interactions is diffractive deep inelastic scattering (DDIS)[3]. DDIS is a deep inelastic scattering reaction with a specific final-state configuration. It was first observed at HERA in 1993 [10]. Two energy scales coexist in this interaction. It is often referred to as a hard diffractive process. It is characterized by a large rapidity gap (LRG) between the proton remnant and the product of the hadronization of the photon. The LRG implies that the virtual photon and the proton do not exchange quantum numbers.

Experimentally, diffractive processes are selected using two characteristics: the presence of the LRG and the presence of one or both incoming particles that remain intact after a collision and are detected by special forward detectors.

Diffractive events in proton-proton interactions include elastic scattering, single dissociation, double dissociation, and central diffractive processes. These processes are schematically depicted in Fig. 1.2. On figure (a) there is a non-diffractive process so the LRG is not present and none of the incoming particles remain intact. On figure (b) there is elastic scattering where there is a significant gap in rapidity and both incoming protons continue after the collision. Single dissociation, and double dissociation are depicted on figures (c) and (d), where in these cases either one or both incoming proton emit new particles which are separated from the other incident particles or its shattering products by the LRG. The double line represents the Pomeron exchange.

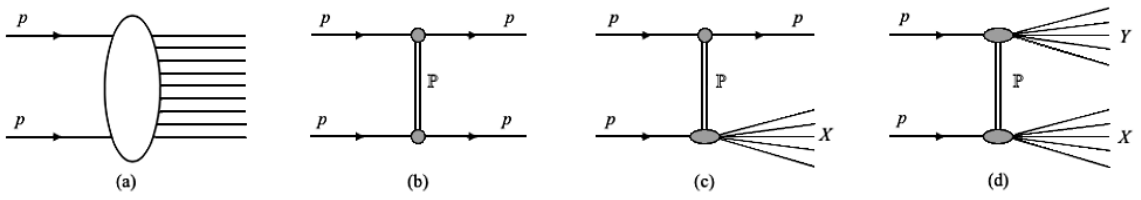

Figure 1.2: Schematics of soft diffractive processes in proton-proton interactions. These include (a) non-diffractive processes, (b) elastic scattering, (c) single dissociation and (d) double dissociation. The double line corresponds to the Pomeron exchange. Taken from Ref. [2].

[3]Deep inelastic scattering (DIS) is a inelastic scattering of a highly energetic lepton on a target hadron. The lepton is deflected. The target absorbs some of the lepton's kinetic energy and for very high energies it can shatter and emit new particles.

All these events have similar properties to those of the well-known optics pattern of diffraction of a beam of light on an obstacle. The term diffraction itself was first used in the context of particle physics by Landau in the 50s. Kirchhoff diffraction theory is indeed formally similar to the quantum theory of potential scattering at high energies. The propagation and interaction of extended objects like hadrons are nothing but the absorption of their wave function caused by the many inelastic channels open at high energy. The next section dives more in-depth into these similarities.

1.2 Optics

The optical analogy has played a crucial role in shaping the research program of heavy-energy diffraction since the 1950s. Kirchhoff's optical theory and the quantum theory of high-energy potential scattering – the Eikonal approximation, have formal similarities. The analogy between particle diffraction and classical optics which is complete in elastic scattering since the internal structure of interacting particles does not come into play, will be thoroughly discussed in this section. First, we derive the cross-section equations from the theory of optics and then in the eikonal approximation to see that they are the same.

1.2.1 Kirchhoff's Theory

In this theory, we begin with the following scenario. A plane wave

$$\varphi(x, y, z, t) = U(x, y, z)e^{-i\omega\ t}, \tag{1.1}$$

where $\omega = ck$ is approaching a screen Σ with a hole Σ_0 of dimension R.

The conditions are that the wave number $k = 2\pi/\lambda$ is sufficiently large so that the short wavelength condition $kR \gg 1$ is satisfied and Helmholtz's equation $(\Delta^2 + k^2)U = 0$ is also satisfied. The modulus squared of U, the intensity of light, equals the energy carried by the wave per time and area.

Before the screen, $U = U_0 e^{ikz}$, where the amplitude of the wave U_0 is constant.

According to the Huygens-Fresnel principle, each point of the hole becomes the centre of a spherical wave. If we have a detector plane at a distance D from the plane to collect the resulting wave from envelopes of the spherical waves. The amplitudes and wavelengths collected at each point of the detector plane will be different as the distances and angles with the original direction of the beam vary. That's why cancellations and reinforcements occur on the detector plane and that is what is called diffraction. Diffraction patterns observed on a detector plane behind a circular hole for two distances D is shown in Fig. 1.3.

The amplitude of the wave is mapped to a value of $U(x, y, z)$ at the point $P(x, y, z)$ on the detector plane as represented in the sketch in Fig. 1.4. Mathematical formula for $U(x, y, z)$ is given by Fresnel-Kirchhoff formula

$$U(x, y, z) = -\frac{\mathrm{i}k}{4\pi} U_0 \int_{\Sigma_0} \mathrm{d}^2\boldsymbol{b}(1 + \cos\chi)\frac{\mathrm{e}^{\mathrm{i}ks}}{s}, \tag{1.2}$$

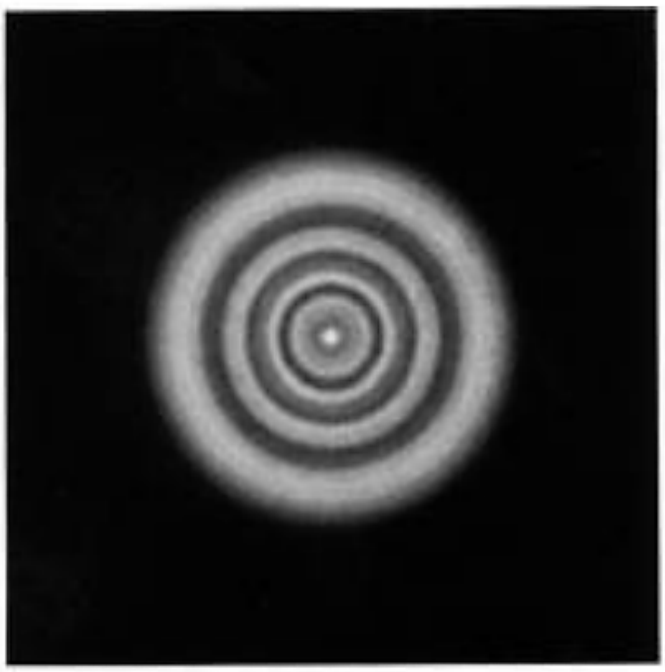

Figure 1.3: Possible diffraction pattern behind a circular hole in a screen. Taken from Ref. [11].

where $\boldsymbol{b} \equiv (b_1, b_2, 0)$ is a vector placed on the plane Σ, s is a vector connecting P to the point of Σ_0 distinguished by $\boldsymbol{b}$, $cos(\chi)$ is the inclination of s with the respect to the normal to Σ. These are depicted in Fig. 1.4 as well.

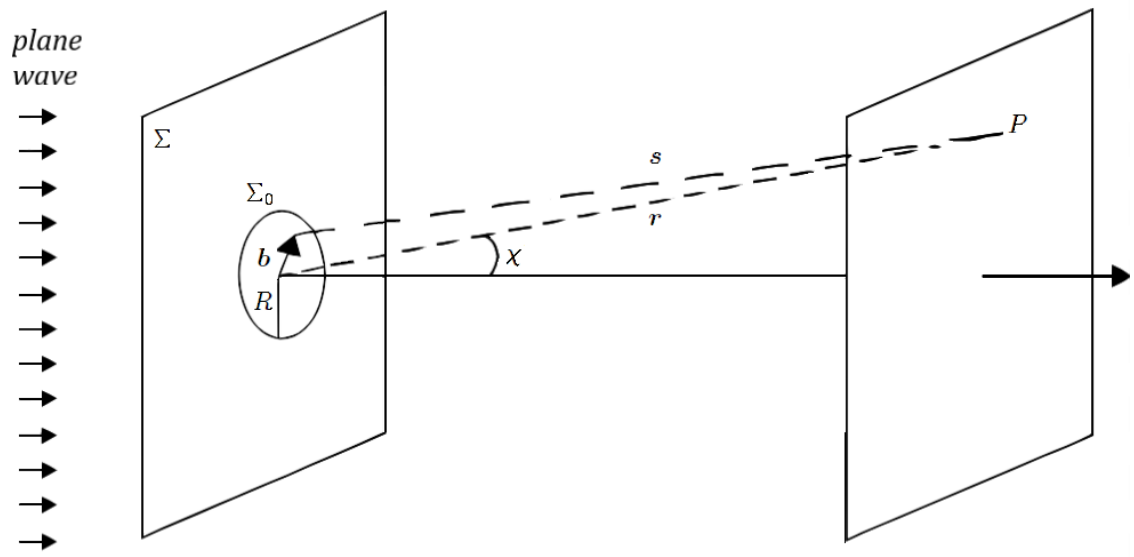

Figure 1.4: Diagram of a diffraction of a plane wave by a hole Σ_0 with the radius R in a screen Σ. Vector s is a vector connecting P to the point of Σ_0 distinguished by $\boldsymbol{b}$, $cos(\chi)$ is the inclination of s with the respect to the normal to Σ. Taken from Ref. [1].

The Fresnel integral (1.2) needs to be calculated. For that the definition of vector $\boldsymbol{r} = \boldsymbol{b} + \boldsymbol{s}$ and the short wavelength condition implying $\cos(\chi) \simeq 1$ is used to

rewrite the integral. Calculation of integral can be simplified in the case of $R/D \ll 1$, the large distance condition. The distance s can be expanded as a power series of b/r.

Further, only the Fraunhofer regime of diffraction is looked into for applying the optical concepts to hadronic phenomena. This regime occurs when $kR^2/D \ll 1$. Two other regimes, which are not considered in this work are the Fresnel diffraction for $kR^2/D \approx 1$ and geometrical optical limit for $kR^2/D \gg 1$.

We take typical values for a hadronic target at an accelerator energy $R \sim 1$ fm, $D > 1$ cm and $k \sim \sqrt{s} \sim 200$ GeV. We can neglect the terms in the expansion of s that are quadratic and higher as the Fraunhofer limit corresponds to the genuine limit of D approaching infinity. We introduce a transverse two-vector, the momentum transfer $\mathbf{q} \simeq \mathbf{k\prime} - \mathbf{k}$, where $\mathbf{k\prime}$ is the outgoing wave vector and $|\mathbf{k}| = |\mathbf{k\prime}| = \mathbf{k}$.

Now the wave function at $P(x, y, z)$ in the Fraunhofer limit is

$$U(x, y, z) = -\frac{\mathrm{i}k}{2\pi} U_0 \frac{\mathrm{e}^{\mathrm{i}kr}}{r} \int \mathrm{d}^2\boldsymbol{b} \Gamma(\boldsymbol{b}) \mathrm{e}^{-\mathrm{i}\boldsymbol{q}\cdot\boldsymbol{b}}, \tag{1.3}$$

where the profile function $\Gamma(\mathbf{b})$ is introduced to extend the integration over the whole plane containing the aperture instead of the surface of hole Σ_0. One simple form of the profile function is

$$\Gamma(\boldsymbol{b}) = \begin{cases} 1 \text{ on } \Sigma_0 \\ 0 \text{ outside } \Sigma_0 \end{cases} \tag{1.4}$$

So far, we considered diffraction by a hole in a screen. The optical analogue of high-energy particle scattering is diffraction by an opaque obstacle. Luckily, we can move towards this problem quite easily considering these principles. Babinet's principle states that a hole and an obstacle of identical form and dimension produce the same diffraction figure. The Huygens-Fresnel principle states that waves diffracted by a hole and an obstacle must combine to reconstruct the incident wavefront.

The amplitude of the wave diffracted by an opaque disc can be obtained by subtracting the plane wave after the hole from the incident wave. This can be written by replacing $S(\mathbf{b}) = \mathbf{1} - \mathbf{\Gamma}(\mathbf{b})$, where the first term represents the unperturbed wave, and the second term yields the diffracted wave. This S is an analogue to the S-matrix in particle physics and describes the modification of a wave to the diffraction obstacle. The S-matrix satisfies a normalisation condition due to energy conservation. From this fact arises its constraint.

The wave amplitude beyond the obstacle is then

$$U(x, y, z) = -\frac{\mathrm{i}k}{2\pi} U_0 \frac{\mathrm{e}^{\mathrm{i}kr}}{r} \int \mathrm{d}^2\boldsymbol{b} S(\boldsymbol{b}) \mathrm{e}^{-\mathrm{i}\boldsymbol{q}\cdot\boldsymbol{b}}. \tag{1.5}$$

Neglecting the constant wave shift of the plane wave we can rewrite the equation for the wave beyond the obstacle as

$$U(x, y, z) = U_{\mathrm{inc}} + U_{\mathrm{scatt}} = U_0 \left(\mathrm{e}^{\mathrm{i}kz} + f(\boldsymbol{q}) \frac{\mathrm{e}^{\mathrm{i}kr}}{r} \right), \tag{1.6}$$

where U_{inc} is the incident plane wave and U_{scatt} is the scattered wave. The factor before the spherical wave term $f(\boldsymbol{q})$ is the physically relevant quantity called the scattering amplitude and it is given by

$$f(\boldsymbol{q}) = \frac{\mathrm{i}k}{2\pi} \int \mathrm{d}^2\boldsymbol{b}\Gamma(\boldsymbol{b})\mathrm{e}^{-\mathrm{i}\boldsymbol{q}\cdot\boldsymbol{b}}. \tag{1.7}$$

The scattering amplitude is the Fourier transform of the profile function introduced earlier. By inverting the Fourier integral we get a formula to substitute back to (1.7) that look as follows

$$\Gamma(\boldsymbol{b}) = \frac{1}{2\pi\mathrm{i}k} \int \mathrm{d}^2\boldsymbol{q} f(\boldsymbol{q})\mathrm{e}^{\mathrm{i}\boldsymbol{q}\cdot\boldsymbol{b}}. \tag{1.8}$$

Finally the scattering amplitude as a Bessel transform of $\Gamma(b)$

$$f(q) = \mathrm{i}k \int_0^\infty \mathrm{d}b b J_0(qb)\Gamma(b), \tag{1.9}$$

where identity $\frac{1}{2\pi}\int_0^{2\pi} \mathrm{e}^{\mathrm{i}x\cos\phi}\mathrm{d}\phi = J_0(x)$ was used.

The differential cross-section $\mathrm{d}\sigma$ is defined using the intensities of incident $I_{\mathrm{i}} = |U_{\mathrm{i}}|^2 = |U_0|^2$ and scattered light $I_{\mathrm{s}} = |U_{\mathrm{s}}|^2 = |U_0|^2|f(\mathbf{q})|^{\mathbf{2}}/\mathbf{r^2}$ as

$$\mathrm{d}\sigma \ = \frac{I_{\mathrm{s}} r^2 \mathrm{d}\Omega}{I_{\mathrm{i}}}. \tag{1.10}$$

Combining this with expressions for I_{i} and I_{i} we can see that the differential cross-section is the modulus squared of the scattering amplitude.

$$\frac{\mathrm{d}\sigma}{\mathrm{d}\Omega} = |f(\boldsymbol{q})|^2. \tag{1.11}$$

By definition, the integrated scattering cross-section is $\sigma_{\text{scatt}} \equiv \int \frac{\mathrm{d}\sigma}{\mathrm{d}\Omega}\mathrm{d}\Omega = \frac{1}{k^2}\int |f(\boldsymbol{q})|^2 \ \mathrm{d}^2\boldsymbol{q}$, where relation $\mathrm{d}^2\boldsymbol{q} = \pi \mathrm{d}q^2 \simeq \pi\,(2k^2\vartheta\ \mathrm{d}\vartheta) \simeq k^2\ \mathrm{d}\Omega$ was used. Finally, from Parseval's theorem

$$\sigma_{\text{scatt}} \ \equiv \int \frac{\mathrm{d}\sigma}{\mathrm{d}\Omega}\mathrm{d}\Omega = \frac{1}{k^2}\int |f(\boldsymbol{q})|^2 \ \mathrm{d}^2\boldsymbol{q}. \tag{1.12}$$

The absorption cross-section, the ratio of the absorbed to the incident energy flux is

$$\sigma_{\text{abs}} = \int \mathrm{d}^2\boldsymbol{b}\left(1 - |S(\boldsymbol{b})|^2\right) = \int \mathrm{d}^2\boldsymbol{b}\left[2\,\mathrm{Re}\,\Gamma(\boldsymbol{b}) - |\Gamma(\boldsymbol{b})|^2\right]. \tag{1.13}$$

By summing the scattering and absorption cross-section, we get the total cross-section

$$\begin{aligned} \sigma_{\text{tot}} &= \sigma_{\text{scatt}} + \sigma_{\text{abs}} \\ &= 2\int \mathrm{d}^2b(1 - \mathrm{Re}\,S(\boldsymbol{b})) = 2\int \mathrm{d}^2b\,\mathrm{Re}\,\Gamma(\boldsymbol{b}). \end{aligned} \tag{1.14}$$

Lastly, combined with the expression for scattering amplitude, the optical theorem is derived. It states that the total cross-section equals the scattering amplitude in the forward direction.

$$\sigma_{\text{tot}} \ = \frac{4\pi}{k}\,\mathrm{Im}\,f(\vartheta = 0) \tag{1.15}$$

Here, this relation comes from the conservation of energy. Analogous relation based on the consequence of probability holds in particle physics.

1.2.2 Potential Scattering – the Eikonal Approximation

Let's now move from the first part of the analogy, the Kirchhoff's optical theory, to the quantum theory of high-energy potential scattering. Potential scattering, more specifically its eikonal approximation, describes the high-energy limit of non-relativistic potential scattering.

In this theory, we begin by searching for a solution to Schrödinger's equation, which describes the relative motion of two spinless particles via potential $V(r)$

$$-\frac{\hbar^2}{2\mu}\nabla^2\psi(\boldsymbol{r}) + V(\boldsymbol{r})\psi(\boldsymbol{r}) = E\psi(\boldsymbol{r}). \tag{1.16}$$

The problem is equivalent to that of the scattering of a particle of mass μ off a fixed potential with a finite range. By introducing $k^2 = 2\mu E/\hbar$ and $U(r) = 2\mu V(r)/\hbar$, the Schrödinger equation becomes $\left[\nabla^2 - U(\boldsymbol{r}) + k^2\right]\psi(\boldsymbol{r}) = 0$.

The starting assumption is that the initial state is a plane wave. In the Eikonal approximation, we take the high/energy limit, where particle energy dominates over interaction potential $E \gg |V(\boldsymbol{r})|$ and the particle wavelength is much smaller than interaction length $k \gg ax$. We assume a solution to the equation (1.16) in the form of a plane wave in the forward direction modulated by some unknown function of $\mathbf{r}$

$$\psi(\boldsymbol{r}) = \varphi(\boldsymbol{r})\mathrm{e}^{\mathrm{i}\boldsymbol{k}\cdot\boldsymbol{r}}. \tag{1.17}$$

By substituting this solution into the simplified Schrödinger equation and neglecting ∇^2 for high-energies as φ and U are expected to be smooth functions of $\mathbf{r}$ and vary only over a distance much larger than $1/k$, we get a simplified equation for φ

$$\left[2\mathrm{i}k\frac{\partial}{\partial z} - U(x,y,z)\right]\varphi(x,y,z) = 0. \tag{1.18}$$

The solution to this equation with the boundary condition $\varphi(x,y,-\infty) = 1$ is

$$\varphi(x,y,z) = \exp\left[-\frac{\mathrm{i}}{2k}\int_{-\infty}^{z} U\left(x,y,z'\right)\mathrm{d}z'\right]. \tag{1.19}$$

The wave function of the scattered particle is then

$$\psi(x,y,z) = \exp\left[\mathrm{i}kz - \frac{\mathrm{i}}{2k}\int_{-\infty}^{z} U\left(x,y,z'\right)\mathrm{d}z'\right]. \tag{1.20}$$

This function does not have a spherical wave behaviour, which is valid for our case of high-energy limit in the small-angle region.

Similarly, as in Kirchhoff's theory, we now decompose the vector $\boldsymbol{r} = \boldsymbol{b} + z\hat{\boldsymbol{u}}_z$, where $\boldsymbol{b}$ is a vector perpendicular to the propagation axis (its length is called the impact parameter). Used vectors are depicted in the sketch in Fig. 1.5. By also using $\boldsymbol{k} = k\hat{u}_z$, we get

$$\psi(\boldsymbol{r}) = \exp\left[\mathrm{i}\boldsymbol{k}\cdot\boldsymbol{r} - \frac{\mathrm{i}}{2k}\int_{-\infty}^{z} U\left(\boldsymbol{b},z'\right)\mathrm{d}z'\right]. \tag{1.21}$$

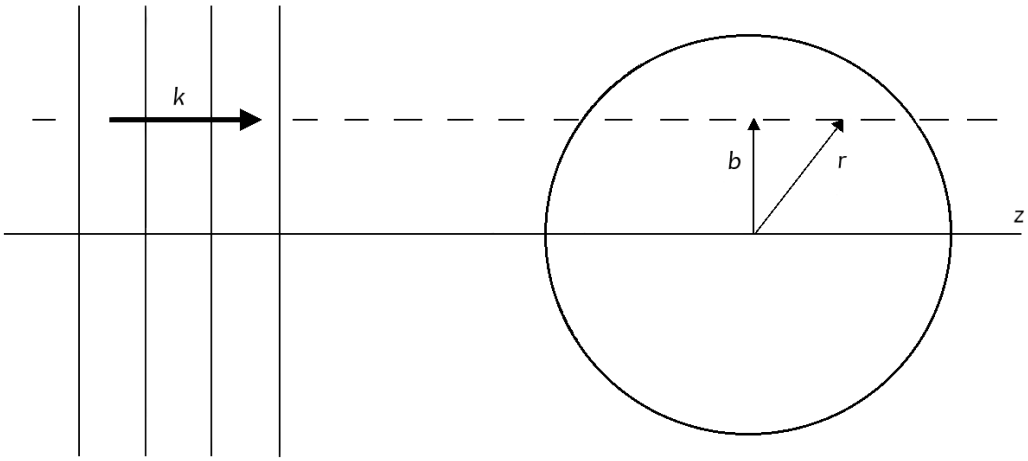

Figure 1.5: Diagram of a plane wave scattering of a potential. Vector $\boldsymbol{b}$ is a vector perpendicular to the propagation axis (its length is called the impact parameter, the vector $\boldsymbol{r}$ is taken as $\boldsymbol{r} = \boldsymbol{b} + z\hat{\boldsymbol{u}}_z$ and $\boldsymbol{k} = k\hat{u}_z$. Taken from Ref. [1].

We want to calculate the scattering amplitude. Approximately, for small scattering angles, the momentum transfer vector is almost orthogonal to the wave number. By recalling $q = 2k\sin\vartheta\ /2$ we get the following expression for the scattering amplitude

$$f(k,\vartheta,\varphi) = \frac{\mathrm{i}k}{2\pi}\int \mathrm{d}^2\boldsymbol{b}\mathrm{e}^{-\mathrm{i}\boldsymbol{q}\cdot\boldsymbol{b}}\left(1-\mathrm{e}^{\mathrm{i}\chi(\boldsymbol{b})}\right), \tag{1.22}$$

where $\chi(\boldsymbol{b}) = -\frac{1}{2k}\int_{-\infty}^{+\infty} U(\boldsymbol{b},z)\mathrm{d}z$ is the eikonal function.

With a strict analogy to optics, we have a quantity called profile function defined as

$$\Gamma(\boldsymbol{b}) \equiv 1 - \mathrm{e}^{\mathrm{i}\chi(\boldsymbol{b})}. \tag{1.23}$$

Again similarly to in the previous section by inverting the Fourier integral of the scattering amplitude we get the profile function in the form of

$$\Gamma(\boldsymbol{b}) = -\frac{2\pi\mathrm{i}}{k}\int \mathrm{d}^2\boldsymbol{q} f(\boldsymbol{q})\mathrm{e}^{\mathrm{i}\boldsymbol{q}\cdot\boldsymbol{b}}. \tag{1.24}$$

We can see that the same relation holds for the profile function in the case of Fraunhofer diffraction (1.8).

The outgoing wave function is then

$$\psi(\boldsymbol{r}) \underset{z\to\infty}{\sim} \mathrm{e}^{\mathrm{i}\chi(\boldsymbol{b})}\mathrm{e}^{\mathrm{i}\boldsymbol{k}\cdot\boldsymbol{r}}, \tag{1.25}$$

where $\chi(\boldsymbol{b})$ represents the phase shift due to scattering.

By some approximations, such as $\mathrm{e}^{\mathrm{i}\chi(\boldsymbol{b})} \simeq 1 + \mathrm{i}\chi(\boldsymbol{b})$ for $\chi(b) \ll 1$ and the Born approximation for the scattering amplitude $f(\boldsymbol{q}) = -\frac{1}{4\pi}\int \mathrm{d}^3\boldsymbol{r}\mathrm{e}^{-\mathrm{i}q\cdot\boldsymbol{r}}U(\boldsymbol{r})$, the scattering amplitude is (analogous to (1.9)).

$$f(k,\vartheta) = \mathrm{i}k\int_0^\infty b\ \mathrm{d}bJ_0(qb)\left(1-\mathrm{e}^{\mathrm{i}\chi(b)}\right), \tag{1.26}$$

where $\frac{1}{2\pi}\int_0^{2\pi}\mathrm{e}^{\mathrm{i}x\cos\varphi}\mathrm{d}\varphi = J_0(x)$.

The expressions for the elastic, inelastic and total cross-sections in the eikonal limit. That they are the same as in optics (1.13), that is

$$\begin{aligned}\sigma_{\text{el}} &= \int \mathrm{d}^2\boldsymbol{b}|\Gamma(b)|^2 \\ \sigma_{\text{in}} &= \int \mathrm{d}^2\boldsymbol{b}\left[2\,\mathrm{Re}\,\Gamma(b) - |\Gamma(b)|^2\right], \\ \sigma_{\text{tot}} &= 2\int \mathrm{d}^2\boldsymbol{b}\,\mathrm{Re}\,\Gamma(b),\end{aligned} \tag{1.27}$$

where $\frac{1}{2\pi}\int_0^{2\pi} \mathrm{e}^{\mathrm{i}x\cos\varphi}\mathrm{d}\varphi = J_0(x)$.

1.3 Kinematics

The Kinematics of scattering processes is an important component of diffractive physics and an essential tool to understand diffraction-based theoretical approaches. The experimental signatures of diffraction are based on the identification of specific kinematic configurations of the final states.

There are mainly two kinds of processes: two-body exclusive scattering $1+2 \to 3+4$ (a special case is elastic scattering $1+2 \to 1'+2'$) and single-particle inclusive scattering $1+2 \to 3+X$, where X represents an unresolved system of particles or a resonance (a special case is single diffractive dissociation $1+2 \to 1'+X_2$).

The number of independent Lorentz-invariant variables for a generic production process $1{+}2 \to 3{+}4{+}\ldots{+}N$ is $4N$, where 4 constraints coming from the conservation of four-momentum $p_1 + p_2 = p_3 + p_4 + \ldots + p_N$, N from mass-shell correction $p_i^2 = m_i^2$, where $i = 1, 2, \ldots, N$ and 6 from fixing 4D reference frame.

1.3.1 Two-Body Processes

The kinematics of two-body reactions is described using Mandelstam variables, which obey the identity[4] $s + t + u = \sum_{i=1}^{4} m_i^2$ and are defined as

$$\begin{aligned} s &= (p_1 + p_2)^2 = (p_3 + p_4)^2 \\ t &= (p_1 - p_3)^2 = (p_2 - p_4)^2 \\ u &= (p_1 - p_4)^2 = (p_2 - p_3)^2 . \end{aligned} \tag{1.28}$$

These equations represent channels, of possible ways to look at interaction as depicted in Fig. 1.6. Reactions depicted on the left most diagram in Fig. 1.6 are referred to as s-channel reactions. The two initial particles "merge" into a virtual intermediate particle that finally splits into the two final particles. The variable s is the square of the total centre-of-mass energy. Analogously reactions depicted on the middle diagram in Fig. 1.6 are referred to as t-channel reactions. The particle 1 emits a virtual particle and in doing so it turns into particle 3. The virtual particle is absorbed by the particle 2, that as a consequence of this interaction turns into

[4]When working with formulas, this thesis uses the natural units of measurement, where the speed of light is exactly one unit, $c = 1$. In the last chapter c is used explicitly in the units of measured quantities, as that is the custom form of results at the STAR experiment.

particle 4. Since the first particle had momentum p_1 before the emission and particle 3 has momentum p_3, the difference of these must have gone into the emitted virtual particle, that thus has (squared) momentum t, the squared momentum transfer. Lastly, reactions depicted on the right most diagram in Fig. 1.6 are referred to as u-channel reactions. As you can see from the image, the u channel is analogous to the t channel with the roles of p_3 and p_4 interchanged. Therefore we can still interpret u as the momentum transfer from particle 1 to particle 2.

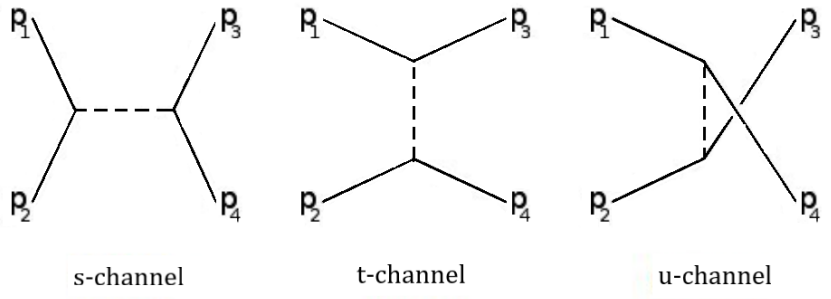

Figure 1.6: Diagrams representing the s, t and u reaction channels and present momenta p_i.

Different channel processes have different and non-overlapping physical domains in the Mandelstam plane (Fig. 1.7) but are described by the same scattering amplitude or by appropriate combinations of the same amplitudes.

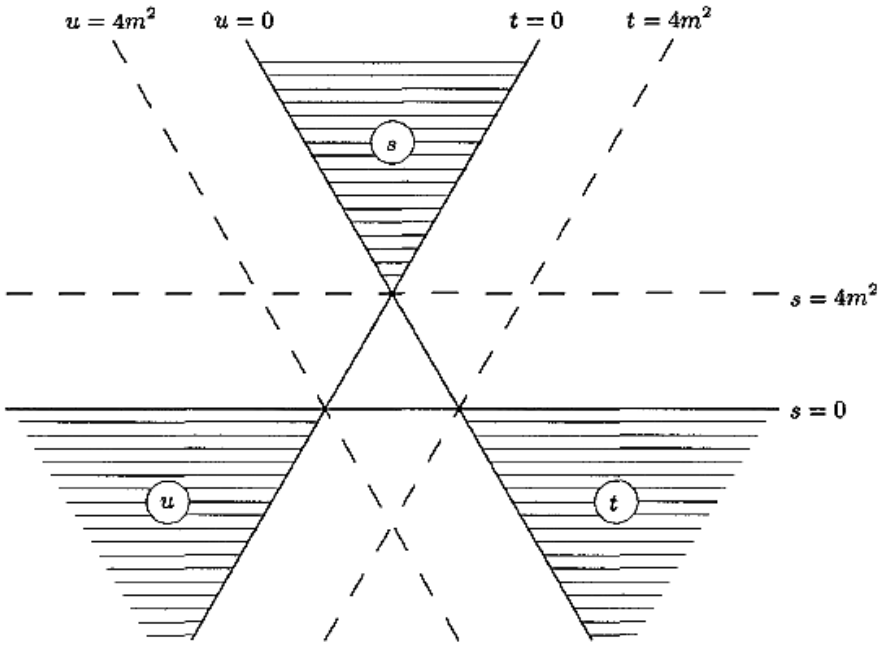

Figure 1.7: The Mandelstam plot showing the physical regions of the s, t and u channels. Taken from Ref. [1].

The kinematics of two-body processes are usually assessed in two frequently used reference systems. That is the centre-of-mass system and the laboratory system. The disappearance of some three-momenta combinations is a characteristic of these systems.

CENTRE-OF-MASS SYSTEM

Take an s-channel reaction taking place with particles 1 and 2 along the z-axis with $p_1 + p_2 = 0$. The scattering angle, ϑ, and the centre-of-mass momentum, p_z, are the only two of the independent four-momentum variables.

$$\begin{aligned} p'_z &= |\boldsymbol{p}'| \cos\vartheta \\ |\boldsymbol{p}_\perp| &= |\boldsymbol{p}'| \sin\vartheta \end{aligned} \tag{1.29}$$

The relation between the centre-of-mass system and the Mandelstam variables is established by expressing the energies of particles in terms of the centre-of-mass energy squared, s, and the relations for momenta from mass-shell conditions. When the masses are neglected for high energies, the energies and momenta are combined to express the Mandelstam variables in terms of the centre-of-mass as follows (using $s + t + u = 4\mathrm{m}^2$)

$$\begin{aligned} s &= 4\left(\boldsymbol{p}^2 + m^2\right) \\ t &= -2\boldsymbol{p}^2(1 - \cos\vartheta) \\ u &= -2\boldsymbol{p}^2(1 + \cos\vartheta). \end{aligned} \tag{1.30}$$

LABORATORY SYSTEM

In this case for the s-channel reaction one of the initial particles is at rest $\boldsymbol{p}_2 = 0$. The Mandelstam variables in terms of laboratory variables at high energies, where masses are neglected are as follows

$$\begin{aligned} s &\simeq 2m_2 E_L \simeq 2m_2 p_L \\ t &\simeq -2m_2 E_4 \\ u &\simeq -2m_2 E_3. \end{aligned} \tag{1.31}$$

1.3.2 Single-Inclusive Processes

Single-particle inclusive reactions are described by three independent variables, usually s, t, and $M^2 = (p_1 + p_2 - p_3)^2$ invariant mass of the X system (missing mass). The Mandelstam variables are described the same as in eq. (1.28) with p_4 replaced by p_X keeping in mind that X is not a real particle. From the same reasoning comes that M^2 is not constant.

Usually to describe single-inclusive processes three variables $[s, x_F, p_\perp^2]$ are used as opposed to $[s, t, M^2]$. The Feynman variable x_F is defined as the ratio of the size of the longitudinal momentum of the outgoing particle to the longitudinal momentum of the incoming particle

$$x_F \equiv \frac{|p'_z|}{p_z}. \tag{1.32}$$

For high-energy limit, where the transverse momentum of a produced particle is small meaning $|p'_z| \simeq p'$ and for $s, M^2 \gg m_i^2, \boldsymbol{p}_\perp^2$, reduces to

$$x_F \simeq 1 - \frac{M^2}{s} \tag{1.33}$$

For a particle of energy E and momentum component p_z along the z-axis, the rapidity y and pseudorapidity η are defined as

$$y = \frac{1}{2} \ln \frac{E + p_z}{E - p_z} \tag{1.34}$$

$$\eta \equiv y|_{m=0} = -\ln \tan \frac{\vartheta}{2}. \tag{1.35}$$

Where pseudorapidity is the same as rapidity for massless particles $E \simeq |\boldsymbol{p}|$ and it is directly related to the angle specifying the direction of motion.

DIFFRACTIVE DISSOCIATION

Diffraction dissociation processes fall in the fragmentation region, where $p_z\prime = p_z$ and. In the specific case of $\gamma^* p$ scattering, with $m_2^2 \to q^2 \equiv -Q^2$, we have

$$x_F \simeq \frac{s - M^2}{s + Q^2}.$$

From the definitions of the Feynman variable (1.32) and (1.33) the longitudinal momentum transfer is $|\Delta\ p_z| \simeq M^2/2\sqrt{(s)}$. The particle produced with $p_z' \simeq p_z$ is called the leading particle and its transverse momentum is related to t by $t \simeq -\boldsymbol{p}_\perp^2$.

1.4 Regge Theory

Exclusive vector meson photoproduction takes place with low photon energies. Virtual quark-antiquark pair's interaction with the target nucleus is thought to occur through an exchange of other mesons or as a result of the combined effect of exchanged mesons called reggeons.

Created in the pre-QCD times the Regge theory was used as a standard theoretical framework for diffraction. It describes the behaviour of scattering amplitudes at high energies $\sqrt{s}$ and small momentum transferred, $-t$. The Regge approach is based on the singularities of amplitudes in the complex angular momentum j plane. Interactions are seen as exchanges of objects called reggeons or Regge trajectories. These are families that mesons make, when the squared of their mass is plotted against their angular momentum. This dependence is represented in the Chew-Frautschi plot [12] in Fig. 1.8, where blue lines represent the Regge trajectories, where red intercepts represent the bound states of particles.

As an example, the measured interaction between negative pion and proton $\pi^- p \to \pi^0 n$ amplitude behaves as

$$T_{\pi p}(s,t) \propto s^{\alpha_\rho(t)},$$

where the complex functions $\alpha(t)$ create poles in the complex plane. The sum of all partial wave amplitudes gives the resulting scattering amplitude along with the total cross section shape. This process is viewed as an exchange of the ρ-trajectory,

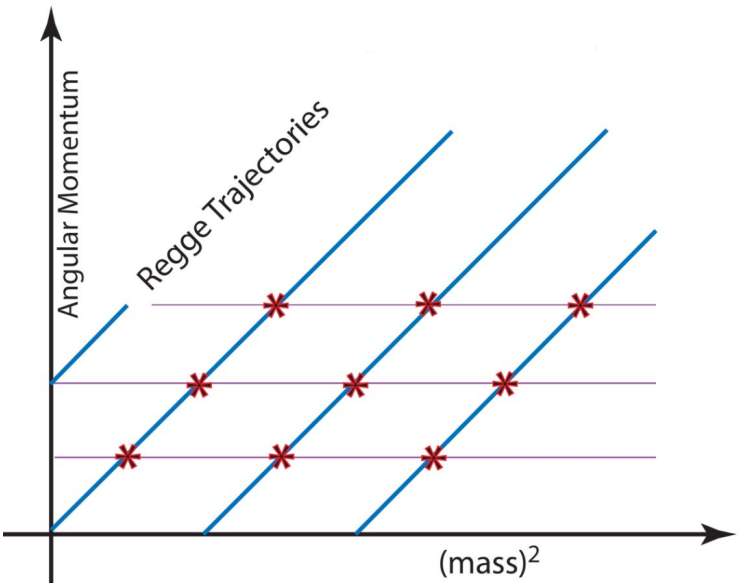

Figure 1.8: The Chew-Frautschi plot of angular momentum as a function of mass squared. Blue lines represent Regge trajectories and red intercepts represent the bound states of particles. Taken from Ref. [13].

$j = \alpha_\rho(t) \simeq 0.5 + 0.9t$ (with $t = (p_{\pi^-} - p_{\pi^n})^2$ in GeV^2). This trajectory passes through the ρ-meson resonance in the 'crossed' t-channel $\pi^-\pi^0 \to \bar{p}n$; that is, $\alpha_\rho\left(t = m_\rho^2\right) = 1$. The corresponding cross-section decreases with increasing s.

On the other hand, high-energy total and elastic pp cross-sections are observed to grow slowly with energy. From the Regge theory perspective, it is dominated by the exchange of a trajectory with vacuum quantum numbers, $\sigma_{\mathrm{tot}} \propto s^{j-1}$. It is assumed that the leading Regge pole at $t \leq 0$, which drives the high-energy behaviour of the cross-section is the rightmost singularity in the j-plane at $j = \alpha(t)$. Then the pp elastic amplitude reads as

$$T_{\mathrm{el}}(s,t) \propto s^{\alpha_{\mathrm{P}}(t)}.$$

By employing the before-derived optical theorem (1.15), the total cross-section can be written as follows

$$\sigma_{\mathrm{tot}} = \mathrm{Im}\, T_{\mathrm{el}}(s, t=0),$$
$$\sigma_{\mathrm{tot}} \propto s^{\alpha_{\mathrm{F}}(0)-1}.$$

Since high-energy total cross-sections were thought to have a constant behaviour, the pole with the largest intercept was originally assumed to be $\alpha(0) = 1$. It is called a Pomeron. The sum of the Pomeron and secondary Reggeons successfully reproduced the energy behaviour cross-section before the LHC. The secondary Reggeon contributions ($\alpha(0) \approx 0.5$) are severely suppressed at Tevatron energies. That allows us to study the Pomeron's properties specifically.

A popular parametrization of the elastic pp scattering amplitude by Donnachie-Landshoff is the Regge form

$$T_{\mathrm{el}}(s,t) = \eta_P \sigma_0 F_1^2(t) s^{\alpha\ \mathrm{RP}}(t),$$

where $\sigma_0 = 21.7$ mb and η_P is the signature factor

$$\eta_P = \frac{1 + \exp\left(-i\pi\alpha_P(t)\right)}{\sin\left(-\pi\alpha_P(t)\right)},$$

F_1 is the Dirac electromagnetic form factor of the proton and the effective Pomeron trajectory

$$\alpha_{\mathrm{P}}(t) = 1 + \Delta + \alpha' t \simeq 1 + 0.0808 + 0.25t$$

with t given in GeV^2. The intercept $\alpha_{\mathrm{P}}(0)$ just above 1 reproduces the observed slow growth of the total hadron-hadron cross-sections at high energies.

At higher energies, this straightforward parametrization, however, becomes progressively less effective. This is due to unitarity, which forces us to consider both the Regge poles as well as the cuts in the j-plane, which correspond to the multiple Regge pole exchanges in the t-channel.

1.5 Photoproduction Cross-Section

One might wonder why the gluon content in protons and nuclei can be effectively probed by vector meson photoproduction. It emerges from the form of the forward scattering cross-section in the two-gluon Pomeron model. The simplest way to view a Pomeron is as a pair of gluons. Even though the running of the strong force coupling constant allows for the use of this internal structure, it does not hold for large values of the strong coupling constant α_S. The interaction energy affects the value of α_S. We operate within the high-energy limit, so it is small. In this model, the forward scattering cross-section takes the form

$$\sigma \ \propto \left[x \cdot g\left(x, \mu^2\right)\right]^2, \tag{1.36}$$

where $g\left(x, \mu^2\right)$ is the gluon density at a given Bjorken x and scale μ. The expression is proportional to the square of the gluon distribution and that is the reason for studying these processes to gain knowledge of parton distribution functions and their modification when bounded in nuclei.

The cross-section for meson exchange decreases with increasing photon energy. At around 30 GeV it reaches its lowest point and starts to increase. This increase is ascribed to the exchange of Pomerons. Pomerons are needed to insert and regulate the colour charges, because even though vector meson photoproduction does not involve colour, the gluons carry it.

A result for cross-section divided by the source to elastic, inelastic and total from data from proton-proton collisions measured at different experiments and for different collisions energies can be seen in Fig. 1.9. The lines in the plot represent the best fit for the data. The minimum at roughly 30 GeV is visible for all the data.

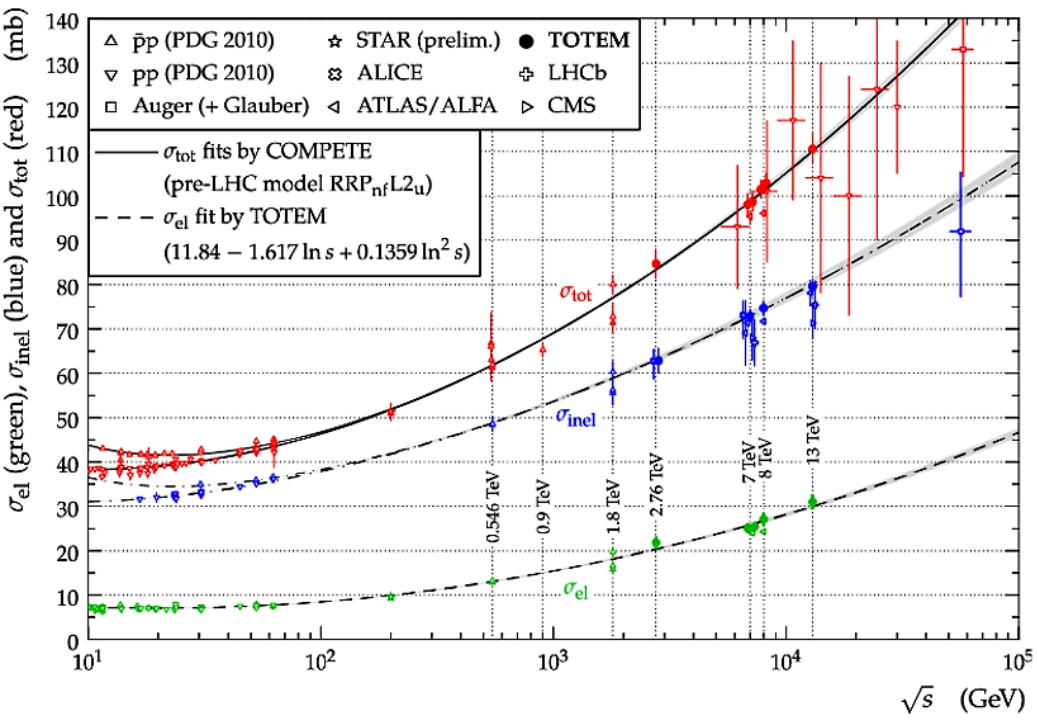

Figure 1.9: Overview of a total, elastic and inelastic cross-section from data from proton-proton collisions from different experiments as a function of $\sqrt{s}$ in red, green and blue respectively. Lines in the plot represent fits to the data. Taken from Ref. [2].

The energy behaviour of $\sigma(q\bar{q}-p)$ is driven by the intercept, $\alpha_{\text{eff}}(0)$, of the effective Pomeron (rightmost singularity in the j-plane), while the value of the cross-section depends on the quark separation, r, in the transverse plane, $\sigma(q\bar{q}-p) \propto \alpha_s^2 \langle r^2 \rangle$. Thus different processes with the same $\langle r^2 \rangle$ are driven by the same $\sigma(q\bar{q}-p)$ cross-section.

First, we look at interaction with a proton as a target. There are two important observations at play in this case. One, at low Bjorken x, the gluon distribution can be described by a power law such as $x \cdot g \propto x^{-\lambda}$, which yields the cross-section $\sigma \propto x^{-2\lambda}$. Second, the kinematic region is $x = \left(M_{\text{V}} c^2 / W_{\gamma\,\text{p}}\right)^2$, where $W_{\gamma\,\text{p}}$ is the photon-proton centre-of-mass energy. Considering both of these statements the cross-section takes the form

$$\sigma \propto W_{\gamma\,\text{p}}^{4\lambda}. \tag{1.37}$$

The production cross-section is non-trivially dependent on W. It increases with W as W^n, where $n = 0.2$ for ρ, ω and ϕ (light quark)-mesons but $n = 0.8$ for J/ψ.

The leading-order QCD predicts that the cross-section for vector meson photoproduction with a proton target should increase a power law with the exponent interpretable in terms of the proton's gluon distribution. This is demonstrated on Fig. 1.10, where cross-section as a function of energy for the reaction γ+p $\to$ J/ψ+p is depicted. The data are taken from measurements at HERA and UPCs at the LHC. The range of Bjorken x values is roughly from 2×10^{-5} to 10^{-2} for the data. It can be seen that the cross-section follows a power law with the exponent $4\lambda = 0.7$, which is comparable to the value obtained in the previous paragraph for J/ψ.

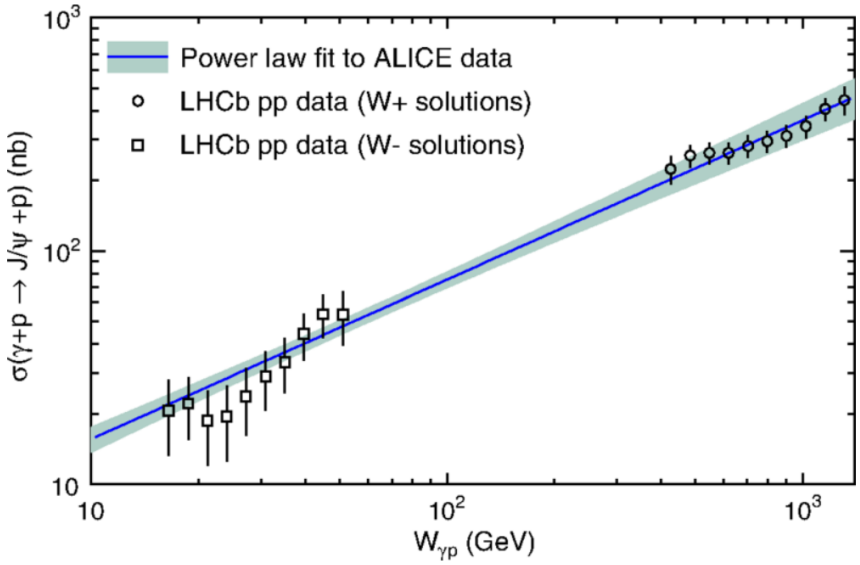

Figure 1.10: Cross-section for the reaction $\gamma + \mathrm{p} \rightarrow \mathrm{J}/\psi + \mathrm{p}$ as function of $W_{\gamma\ p}$. Data are from *pp* collisions from the LHCb experiment. Blue line and band represent power law fit to ALICE data. Taken from Ref. [14].

Now we investigate the same process but for heavy-ion targets. There must be some adjustments made to account for the numerous bound protons and neutrons inside. But how are nucleons altered when near one another. It was established that the parton distribution functions of bound and unbound nucleons differ. Although no precise measurements have been made to support it, there may be some processes at work, such as gluon saturation.

Based on the previous findings for proton targets, it is possible to estimate the cross-section for the photoproduction off heavy nuclei. The phases of amplitudes for the Pomeron to interact with each target nucleon are the same if the momentum transferred by the Pomeron is low enough. The cross-section scales as A^2 in that case. It should be considered that the quark-antiquark pair might interact more than once when going through the nuclei. This would still result in a single vector meson, but the cross-section may increase slower, particularly in processes that lead to lighter vector mesons.

DIFFRACTION PATTERNS

Distributions of nucleons within the target nucleus are determined rom the observable diffraction patterns within the cross-section distributions. Distinct diffractive dips in the cross-section for the production of ρ^0 mesons are visible on Fig. 1.11.

Similar to the result in the previous figure, Fig. 1.12 of the t dependence of the *pp* elastic cross-section from TOTEM data also shows a clear diffraction dip at 0.5 GeV^2. It can also be seen that the diffractive dip moves to smaller values with increasing energy, which comes from the so-called geometrical scaling model.

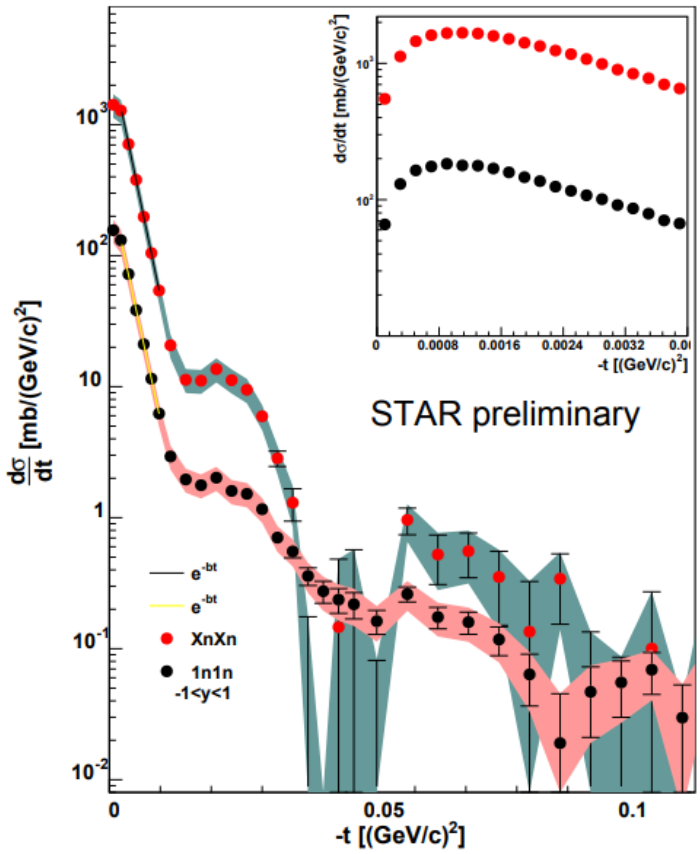

Figure 1.11: Cross-section for ρ^0 photoproduction as a function of $-t$ with visible diffraction dips. Taken from Ref. [15].

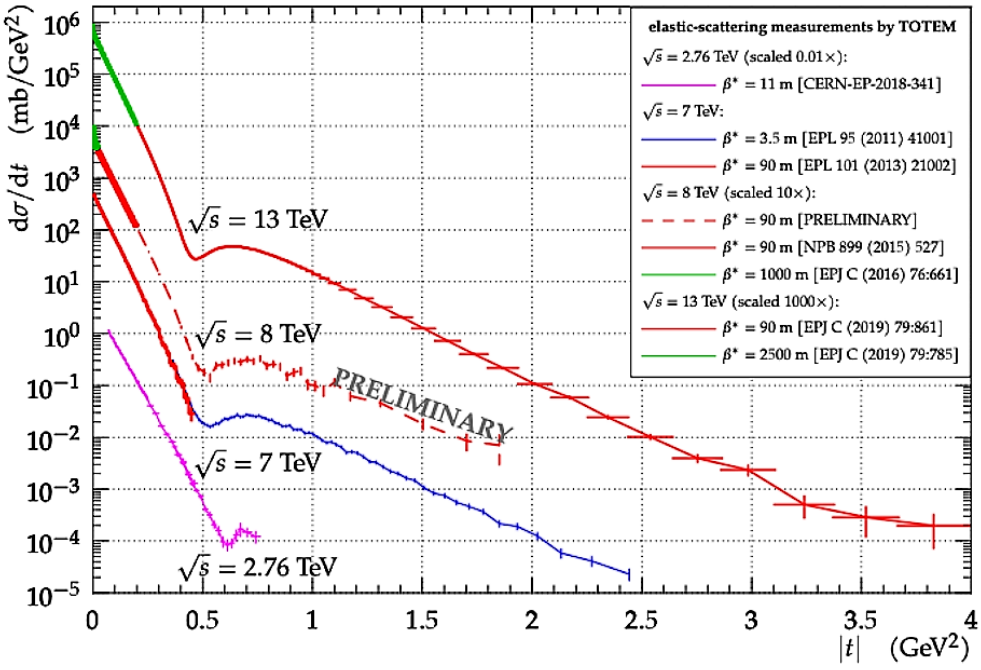

Figure 1.12: The t dependence of the pp elastic cross-section with visible diffractive pattern for different collision energies. Taken from Ref. [2].

INTERFERENCE

A single ion pair can exchange multiple photons in a single encounter due to the strong electromagnetic fields connected to UPCs. These photons have the same impact parameter despite being independently emitted. A two-source interferometer is formed by the initial state of UPC, which has two identical nuclei that are indistinguishable from one another. The propagation from nucleus 1 to nucleus 2 must be taken into account by adding the quantum mechanical amplitudes with a phase factor because the two outcomes of interaction produce indistinguishable final states. As a result the cross-section scales as

$$\sigma \propto |A_1 - A_2 \exp\left[(i\mathbf{p}_{\mathrm{T}} \cdot \mathbf{b})/\hbar\right]|^2 . \tag{1.38}$$

Here A_1 and A_2 are the amplitudes for the two possibilities from above, p_{T} is the vector meson transverse momentum and $\mathbf{b}$ with the magnitude b is the impact parameter vector parallel to the photon polarization. The exponential term is the propagation phase factor.

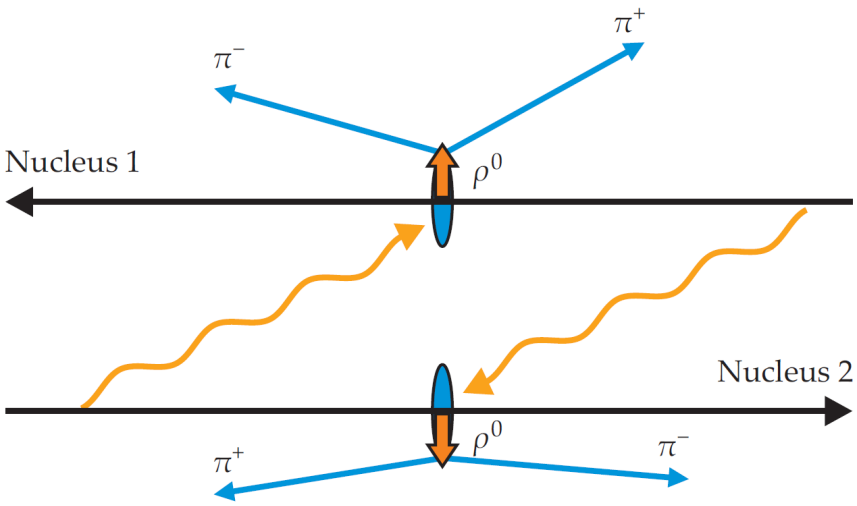

Figure 1.13: Diagram showing two possible interactions between two incident nuclei resulting in interference.Taken from Ref. [3].

The final-state vector meson's longitudinal momentum partly controls the amplitudes A_1 and A_2. When the vector mesons have no longitudinal momentum in the centre-of-mass frame of reference, as in Fig. 1.13, the amplitudes are equal. The cross-section is suppressed in that scenario when $p_{\mathrm{T}} < \hbar/b$. More specifically, at low p_{T} the derivative $d\sigma/dp_{\mathrm{T}}^2$ is proportional to p_{T}. And the derivative would tend to be a constant if interference didn't exist. Plot in Fig. 1.14 shows that the derivative does indeed drop at small p_{T}.

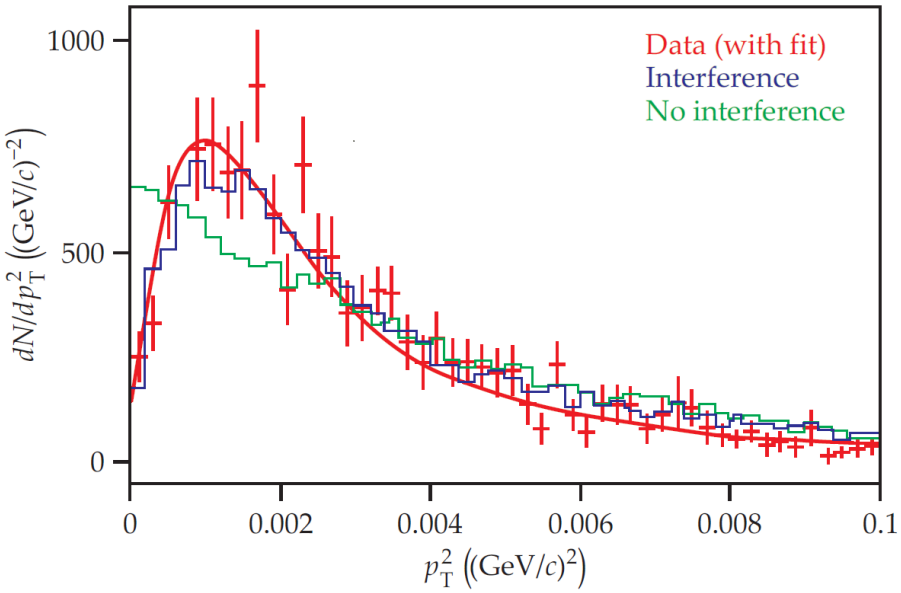

Figure 1.14: Interference measured by STAR in heavy-ion UPCs. Taken from Ref. [3].

Chapter 2

Recent Results from Photoproduction of J/ψ

High-energy physics is a fast-evolving field. This chapter concentrates on presenting as up-to-date results as possible while relating them to the information introduced in the first chapter of this work. Results of new measurements of J/ψ and other vector mesons in UPCs through diffractive phenomena in the last 5 years by different collaborations, encompass a range of collision systems and energies and are summarized. These results originate from experiments conducted at the ALICE detector at the Large Hadron Collider (LHC) and the STAR experiment at Brookhaven National Laboratory (BNL). Other experiments not mentioned in this section, such as those at the CMS detector at the LHC and the PHENIX experiment at BNL, have also contributed valuable insights into understanding the properties of particles under extreme collision conditions.

2.1 ALICE Measurement

In 2019 ALICE collaboration measured the energy dependence of exclusive J/ψ photoproduction off protons in pPb UPCs at centre-of-mass energy $\sqrt{s_{\mathrm{NN}}} = 5.02\,\mathrm{TeV}$ [16]. Presented is the J/ψ photoproduction cross-section of e^+e^- and $\mu^+\mu^-$ decay channels. These are comparable with previous results as well as theoretical models and show the expected power-law behaviour.

This measurement also serves as a tool to look for proof of gluon saturation effects, for which there is no evidence so far. Gluon saturation effects are the most simple mechanism that could cause the behaviour of the probability distribution function for gluons at very high energies. The gluon structure function in protons rises rapidly at small values of Bjorken x corresponding to the high-energy limit of QCD. To satisfy unitarity constraints this growth has to stop. At leading order pQCD, the cross-section for this process depends on the square of the gluon density in the target so saturation effects. Calculations within pQCD are possible from the large enough mass of the charm quark so the exclusive photoproduction off protons is a good probe.

The measurements are performed in three rapidity intervals: semi-backward ($-2.5 < y < -1.2$), mid ($|y| < 0.8$) and semi-forward ($1.2 < y < 2.7$). At midrapidity, the J/ψ candidates decay into lepton pairs detected with ALICE central barrel detectors. In the other two rapidity intervals, J/ψ decays into a muon pair where one is measured with the muon spectrometer and the other with the central barrel detectors.

The value of the photon-proton centre-of-mass energy is calculated from $W^2_{\gamma\ \mathrm{p}} = 2E_{\mathrm{p}}M_{\mathrm{J}/\psi}\exp(-y)$, where $M_{\mathrm{J}/\psi}$ is the J/ψ mass, $E_{\mathrm{p}} = 4$ TeV is the energy of the proton beam and y is the rapidity of J/ψ measured in the laboratory frame w.t.r. to the direction of the proton beam. Hence in this measurement the $W_{\gamma\mathrm{p}}$ range from 40 to 550 GeV.

The cross-section for the exclusive J/ψ production of protons with lead nuclei is computed as

$$\frac{\mathrm{d}\sigma}{\mathrm{d}y} = \frac{N_{\mathrm{J}/\psi}}{\varepsilon \times \mathrm{A} \cdot \mathrm{BR}\,(\mathrm{J}/\psi \to l^+l^-) \cdot L_{\mathrm{int}} \cdot \Delta\ y}, \tag{2.1}$$

where Δy represents the width of the rapidity region where the measurement is performed and the branching ratios are $\mathrm{BR}\,(\mathrm{J}/\psi \to \mathrm{e}^+\mathrm{e}^-) = (5.97 \pm 0.03)\%$ and $\mathrm{BR}(\mathrm{J}/\psi \to\ \mu^+\mu^-) = (5.96 \pm 0.03)\%$. The values to be put into this equation were measured and computed during the analysis.

Then to be able to compare their measurement with other results the cross-section for exclusive photoproduction of J/ψ off protons is calculated as

$$\frac{\mathrm{d}\sigma}{\mathrm{d}y} = k\frac{\mathrm{d}n}{\mathrm{d}k}\sigma(\gamma + \mathrm{p} \to \mathrm{J}/\psi + \mathrm{p}), \tag{2.2}$$

where $k = 0.5 \times M_{\mathrm{J}/\psi}\exp(-y)$ is the photon energy in the laboratory frame and $k\ \mathrm{d}n/\mathrm{d}k$ the flux of photons with energy k emitted by the lead nucleus.

The final measurements are shown in Fig. 2.1 where the exclusive photoproduction cross-section of J/ψ as a function of W is plotted. The presented range of W corresponds to about three orders of magnitude of x. The plot shows a fit of a power law $N\,(W_{\gamma\ \mathrm{p}}/W_0)^{\delta}$ to the data with starting parameter $W_0 = 90.0$ GeV and found parameters: $N = 71.8 \pm 4.1$ nb, $\delta = 0.70 \pm 0.05$. These are comparable with previous ALICE and HERA measurements.

The data presented here, augmented with the results from future measurements, will be a powerful tool to better understand the role of saturation at the highest energies.

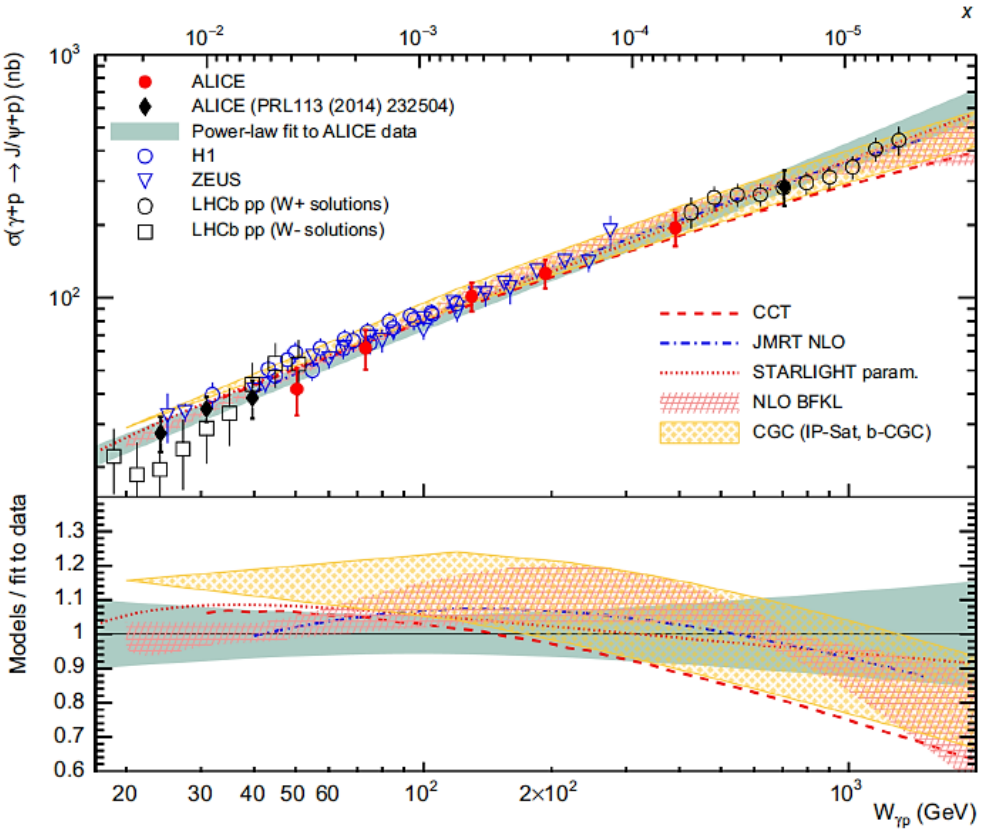

Figure 2.1: Exclusive photoproduction cross-section of J/ψ as a function of W with a power-law fit. Data are taken from several experiments. Coloured bands represent different model predictions. Taken from Ref. [16].

2.2 STAR Measurement

The most recent paper to be summarized in this chapter is a 2022 report from STAR collaboration on J/ψ photoproduction in dAu UPCs focusing on probing the gluonic structure of the Deuteron [17].

Deuteron was selected in this measurement being the simplest nuclear bound state to provide insight into the gluon density distributions, the nuclear breakup process and the nuclear gluonic structure. It is not predicted for gluon saturation or the nuclear shadowing effect to have a substantial impact as the Bjorken x for STAR kinematics is approximately 0.01. This allows us to understand the interplay between coherent and incoherent vector meson production. The coherent interaction may be distinguished by looking for neutrons from deuteron decay following a photon-deuteron interaction in the deuteron-going direction. The term n-tagged data is used for the coherent interaction data because of this.

The neutron-tagged data in the deuteron-going zero-degree calorimeter are being examined for the first time within this analysis. In the energy ranges present for this analysis the momentum transfer is approximated by transverse momentum squared of J/ψ particles $-t \approx \mathrm{p}^2_{\mathrm{TJ}/\psi}$. Approximate photon-nucleon centre-of-mass energy is $W = 25$ GeV.

Ratio between differential cross-section of J/ψ photoproduction as a function of $-t$ and photon deuteron cross-section

$$\frac{d^2\sigma^{(d+\mathrm{Au}\to J/\psi+X)}}{dtdy} = \Phi_{T,y}\frac{d^2\sigma^{(y^*+d\to J/\psi+X)}}{dtdy}, \tag{2.3}$$

where $\Phi_{T,y}$ is the average transversely polarized photon flux emitted from Au nucleus. As the probability of a photon emitted by deuteron is 4 orders of magnitude smaller it is negligible in this analysis with J/ψ rapidity. X denoted deuteron (coherent) or deuteron-dissociative (incoherent) system.

Then the full differential cross-section in the photon-deuteron system can be written as

$$\frac{d^2\sigma^{(y^*+\mathrm{d}-J/\psi+x)}}{\mathrm{d}t\mathrm{d}y} = \frac{1}{\Phi_{T,y}}\frac{N_{\mathrm{obs}}}{\Delta\ t\times\Delta\ y\times(A\times\epsilon)\times\epsilon_{\mathrm{trig}}}\times\frac{1}{L_{\mathrm{int}}\times\mathrm{BR}\,(e^+e^-)}, \tag{2.4}$$

where $\Phi_{T,y} = 11.78$ based on the STARlight Monte Carlo generator, N_{obs} is the raw J/ψ yield, L_{int} is the integrated luminosity[1], BR = 5.93% is the branching ratio ofJ/ψ decaying into an electron pair, Δt is bin width of $p^2_{\mathrm{T,J}J/\psi}$, and $\Delta y = 2.0$ is the is the rapidity range, $A\times\epsilon$ is the J/ψ reconstruction acceptance and efficiency corrections, and ϵ_{trig} is the trigger efficiency correction. This result is shown on Fig. 2.2 with full data differentiated from n-tagged data, which require a neutron to be detected in the deuteron-going ZDC detector from the deuteron breakup.

The three main physics processes that contribute to the cross-section seen are: coherent diffraction that preserves the integrity of the deuteron, incoherent diffraction with elastic nucleon ($X = p + n$), and incoherent diffraction with nucleon dissociation ($X = p(n)$ + fragments. The higher the J/ψ energy, the smaller of the fraction is n-tagged data.

The final differential cross-sections for full data and the n-tagged data as a function of momentum transfer $-t$ are compared to the colour glass concentrate (CGC) saturation model and the leading twist approximation (LTA) modes. The CGC model provides a better qualitative description of the data. A specific comparison to models separating coherent and incoherent process contributions for the data is shown in 2.3. For coherent processes, both models predict a similar slope. At low $-t$ the incoherent predictions are significantly different. Presented is the first direct measurement of incoherent diffractive J/ψ production at low $-t$ using the n-tagged data. Results are in better agreement with incoherent prediction based on the CGC model.

Results from this paper represent the pivotal experimental starting point for the upcoming high-precision measurement of diffractive J/ψ production at the Electron-Ion Collider. Significant experimental restrictions on deuteron gluon density distributions and the deuteron breakup process are imposed by data and model comparisons.

[1]Integrated luminosity is the integral of the luminosity with respect to time. In scattering theory and accelerator physics, luminosity is the ratio of the number of events detected in a certain period of time to the cross-section.

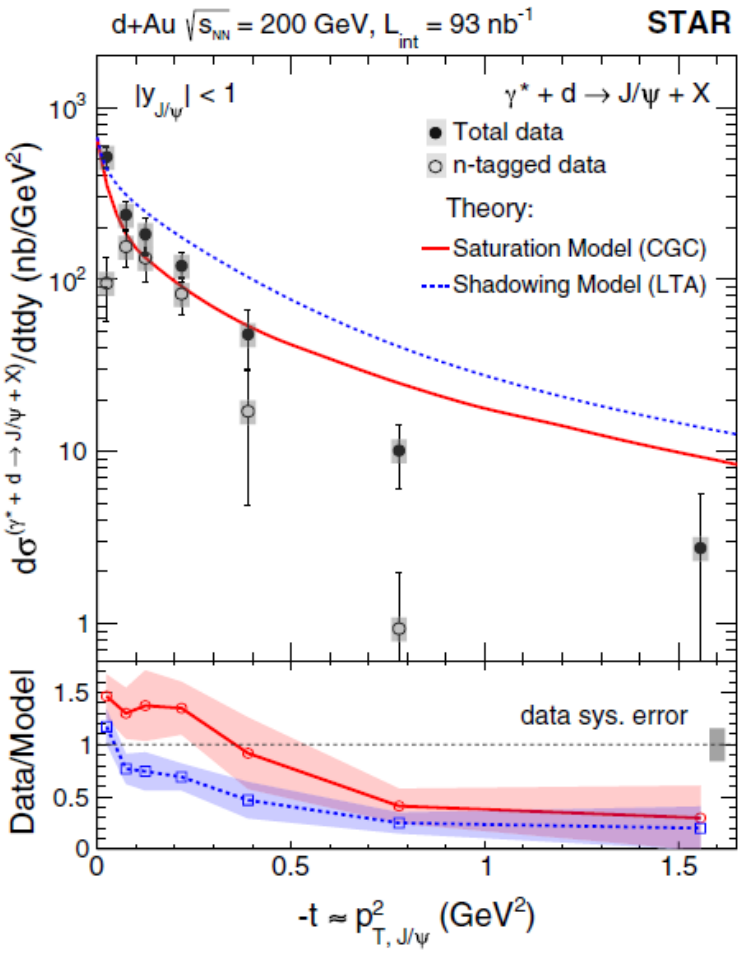

Figure 2.2: Full differential cross-section of photon-deuteron system as a function of $-t$ with n-tagged data differentiated. Red and blue lines and bands represent model predictions from the Saturation model and Shadowing model. Taken from Ref. [17].

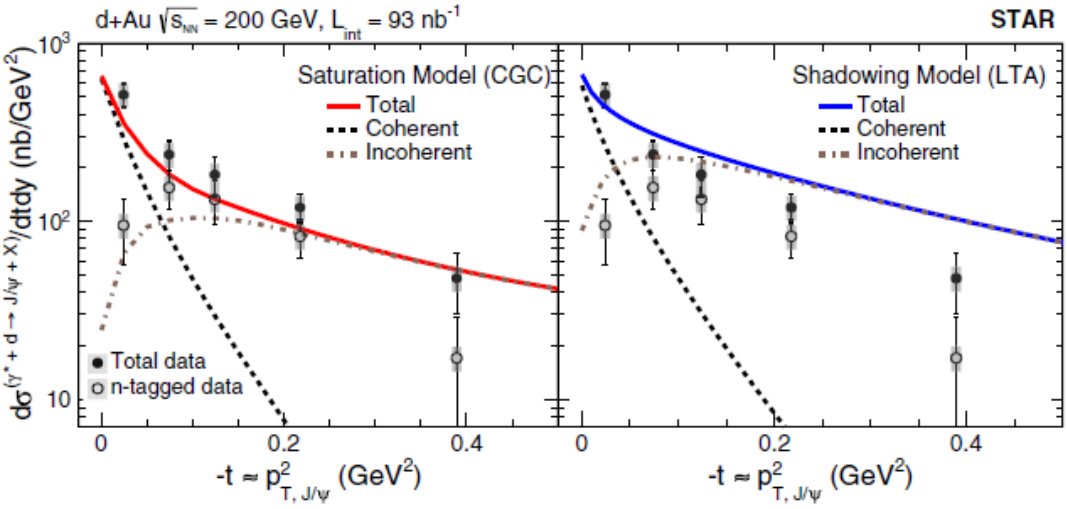

Figure 2.3: Full differential cross-section of photon-deuteron system as a function of $-t$ with n-tagged data differentiated. Left and right panel represent different models: Saturation model and Shadowing model. Coherent and incoherent model predictions are shown for both panels. Taken from Ref. [17].

Chapter 3

Reconstruction of J/ψ in pp $\sqrt{s} = 510$ GeV Data

In this chapter I present results of my analysis work. The code for the analysis is based on templates provided by my supervisors and and the code I used for analysis in my Bachelor thesis. The distribution plots shown in this chapter are my own work. The analysis is in progress and figures with label "This work" represent the result in progress and they were not approved by the STAR collaboration for public presentation.

The goal for this thesis is to study the J/ψ photoproduction with tagged forward proton in pp collisions at $\sqrt{s} = 510$ GeV at the STAR experiment. It is the first analysis of this type with the possibility to measure the forward protons in Roman Pots. This allows to compare the outcomes before and after applying criteria to the forward proton. In the end we are interested in the cross-section of the process as the function of the transferred momentum $-t$ and the exploration of the possibility to determining the transverse momentum of the virtual photon involved in this process.

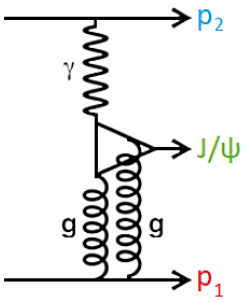

Figure 3.1: Diagram of exclusive J/ψ photoproduction in ultraperipheral pp collision. One proton (p_2 in the diagram) with low p_T interacts via a photon that fluctuates to a virtual hadronic state – a quark-antiquark pair. The other proton (p_1) with high p_T acts as a target to the photon and interacts via the exchange of Pomeron represented by the two gluons. It is left intact during this interaction. J/ψ is reconstructed through its decay channel into an electron-positron pair.

Fig. 3.1 shows a diagram of the investigated process, exclusive vector meson photoproduction in UPC of protons. One proton (p_2 in the diagram) with low p_T interacts via a photon that fluctuates to a virtual hadronic state – a quark-antiquark pair. This proton scatters at a small angle and is not measured. The other proton

(p_1) with high p_T acts as a target to the photon and interacts via the exchange of Pomeron represented by two gluons. It is left intact during this interaction. It scatters and is measured in Roman Pot detectors. The electron and positron used to reconstruct J/ψ are detected in the central barrel detector of STAR.

Conservation of momentum and subsequently also of transverse momentum p_{T} applies in these collisions $\left(\mathbf{p}_1 + \mathbf{p}_2 + \boldsymbol{p}_{\mathrm{J}/\psi}\right)_{\mathrm{T}} = 0$. Hence, since we measure transverse momenta of the final-state electron and positron, and the Pomeron-side proton, we can use them to obtain p_T of the virtual photon from formula $-\boldsymbol{p}_{2,\mathrm{T}} = \left(\boldsymbol{p}_1 + \boldsymbol{p}_{\mathrm{J}/\psi}\right)_{\mathrm{T}}$. The size of this vector is sometimes called the missing p_{T} as it represents the unmeasured transverse momentum in the interaction. Given that the momentum is predicted to be very small, the STAR detector resolution may be the limiting constraint of this measurement. This analysis can at least provide a value's upper limit in that case.

3.1 The Experimental Set-up

For my analysis I used data from *pp* collected in 2017 by the Solenoidal Tracker at RHIC (STAR [18]). As shown in Fig. 3.2, it is one of the experiments located on the Relativistic Heavy-Ion Tracker (RHIC [19]) at Brookhaven National Laboratory (BNL [20]). Data collection began in 2000 with the goal of examining the characteristics of heavy-ion collisions and the quark-gluon plasma (QGP). It can now also be used to measure proton-proton collisions or collisions with a fixed target thanks to years of continuous advancements. Forward detectors were installed in 2009, initially as part of a separate experiment called PP2PP [21], to detect forward protons exiting with a small deviation from the z-axis.

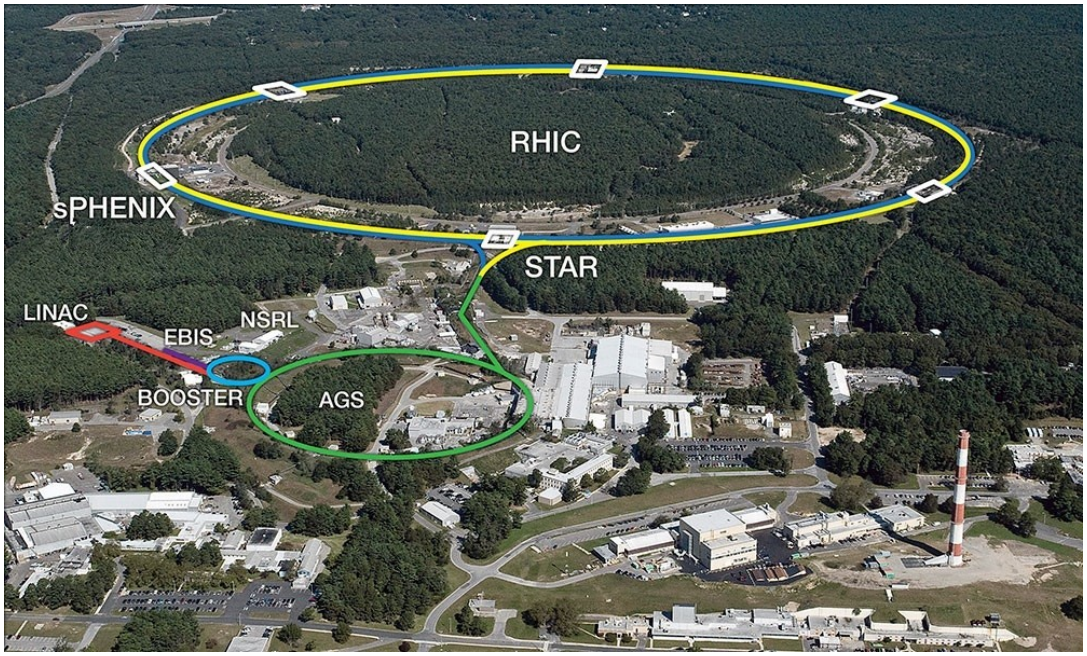

Figure 3.2: Schematic view of the RHIC accelerator complex with its pre-accelerators and the two currently running experiments STAR and sPHENIX. Taken from Ref. [20].

The layout of the experimental set-up is shown Fig. 3.3. The approximately cylindrical central STAR detector is situated in the middle with its main z-axis parallel to the beam line. STAR has many subdetectors and their make-up varies over time. The structure from the year 2017 is displayed in Fig. 3.4. Detectors relevant for this analysis are TPC, BBCs, ZDC and BEMC in addition to RP detector system.

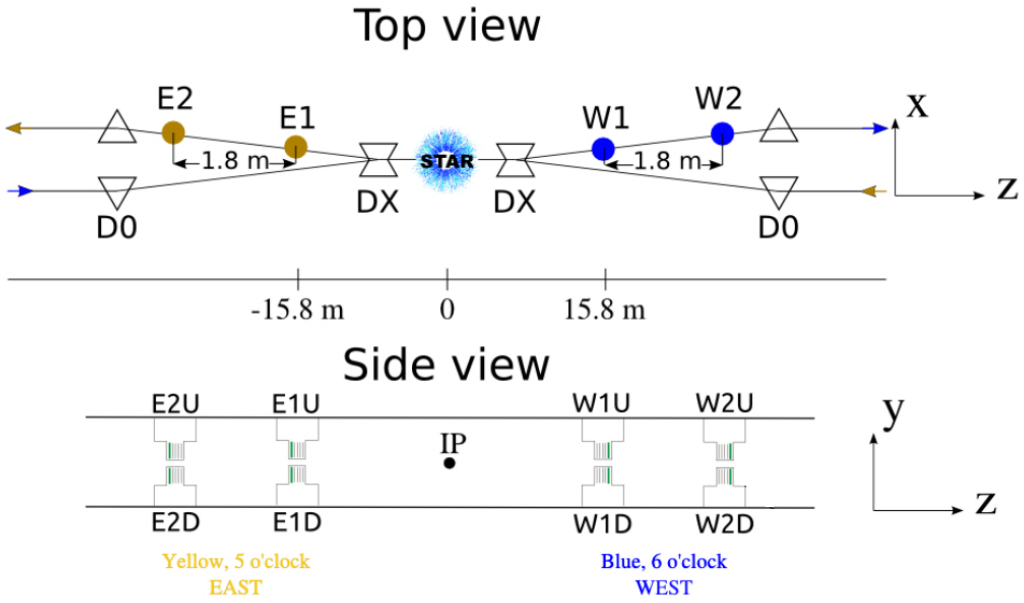

Figure 3.3: Layout of the experimental set-up. Top view on the upper plot and side view on the bottom plot. The central STAR detector in the middle and the four RP stations depicted as E1, E2, W1, W2. Dipole magnets depicted as DX and D0. Taken from Ref. [22].

Time Projection Chamber (TPC) [23]
TPC is a cylinder-shaped detector with radii of 0.5 m and 2.0 m and with a length of 4.2 m developed for the purpose of detecting and tracking charged particles. Detection of charged particles is possible in the entire azimuthal range of angles. Pseudorapidity coverage for central tracking is approximately three units approximately from -1.5 to 1.5. Its cross-section is depicted in Fig. 3.4. The cylinder is filled a gas mixture of argon 90 % and methane 10 % at 2 mbar over atmospheric pressure. In the middle is a membrane with the voltage -28 kV, hence the electric field along the z-axis is 140 V cm^{-1}.

A charged particle passing through the detector ionizes the gas. Positive ions travel to the inner membrane and the faster electrons to the anodes at the ends of the cylinder. Electrons drift time is around 40 μs. If the event passes through the trigger the electrons are let through the gated grid dividing the main volume and the multi wire proportional chambers (MWPC) at the ends of the cylinder. In this space electrons trigger avalanche charge multiplication. These secondary electrons are detected in the MWPCs. The position of creation is determined by the flight time of the electron. From the position measurement, the TPC is able to determine charged particles momenta and identify them in the momentum range of 100 MeV/c to 1 GeV/c. The momentum and the charge of a particle are determined from the curvature of the track. The TPC provides an information about the number of electrons in each hit, which is proportional to the amount of ionization energy loss of the particle traversing the TPC volume. This helps with particle identification.

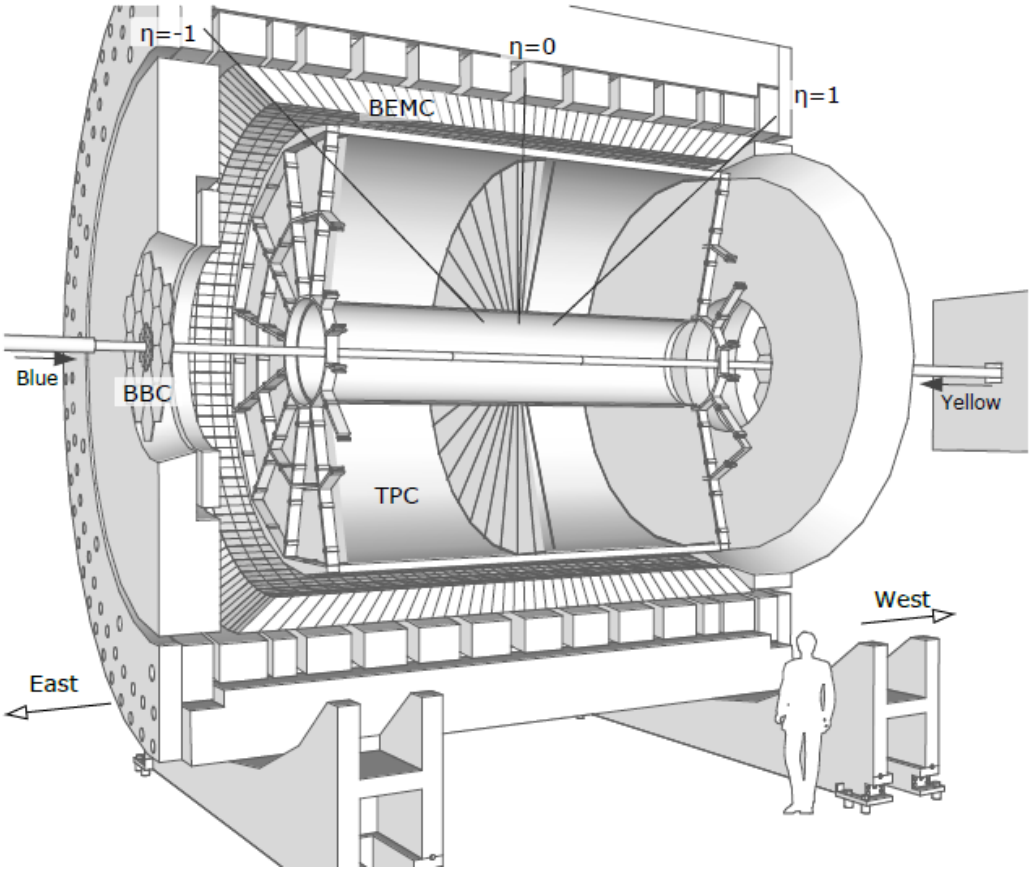

Figure 3.4: Cross-section of the STAR detector showing its beamline and subdetectors TPC, BEMC, BBC. Taken from Ref [19].

Beam Beam Counter (BBC) [24]
One BBC is placed on both end caps of the central barrel 3.75 m from the centre. These detectors measure the location of an interaction vertex that is used in triggering and provide input to the triggering system. They cover a pseudorapidity region from 2.2 to 5.0. Each BBC consists of 18 small and 18 large scintillator tiles. The coincidence between BBC modules serves as the main minimum bias trigger used for proton-proton collisions. In addition, BBCs provide the information about luminosity and polarization of the beams.

Barrel Electromagnetic Calorimeter (BEMC) [25]
Situated on the outer side of the TPC cylinder, it covers the full azimuthal angle. It is made out of 120 modules each made out of 40 towers (4800 in total). The towers are oriented in the direction of the particle's flight so that they fall perpendicularly. Charged particles in the detector lose their energy, which is used for energy and time measurement. BEMC is a sampled calorimeter consisting of two materials: 20 layers of thick lead absorbent plates and 21 scintillation plates.

Roman Pot Detector System (RP) [21]
Away from the central barrel are the Roman Pot detectors. This system of detectors is composed of four stations, two on each side of the central STAR detector at a distance of 15.8 m and 17.6 m. There are two Roman Pots at each station, one above and one below the beam line. The naming convention denotes the position of each detector in the RP system: E(east) or W(west) depending on the side of the interaction point, 1 or 2 to differentiate the two stations on each side, and U(up) or D(down) based on the position with the respect to the beamline.

Detail of one Roman Pot and its inside structure is depicted in Fig. 3.5 and 3.6. Each RP is composed of four silicon strip detectors, where two are oriented horizontally and two vertically. In RP they alternate and form a grid, with the help of which the position of the passing proton in the transverse plane is measured. The active area of the SSD detectors with a strip pitch of about 100 mm is approximately 79 $\times$ 48 mm^2. In addition to the SSDs, each detector assembly includes a scintillator (8 cm $\times$ 5 cm) combined with two photomultipliers, that provide fast signal for triggering of forward scattered protons and information about the time of flight.

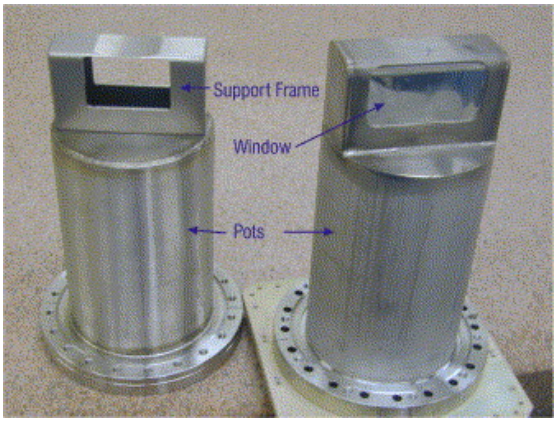

Figure 3.5: A Roman Pot vessel. Taken from Ref [21].

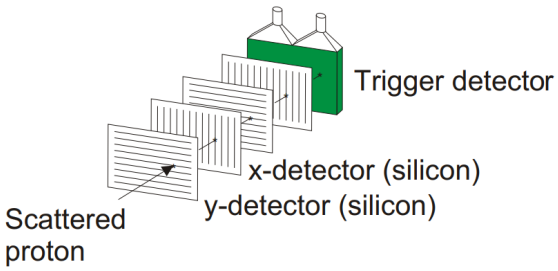

Figure 3.6: Inside structure of the RP detector. Taken from Ref [26].

3.2 Data and event selection

As it was already mentioned, in this work I am analysing data from proton-proton collisions at the energy $\sqrt{s} = 510$ GeV collected in 2017. Data for this are in the UpcDst format, which is the classical STAR PicoDst format modified to include information about the forward protons, in which at the beginning includes 1.17 billion events.

The data for this analysis is stored in the star-UpcDst format (for analyses dealing with central and ultra-peripheral collisions) created by my older colleagues from the faculty, Ing. Jaroslav Adam, Ph.D. and Ing. Tomáš Truhlář. It is an alternative to the PicoDst format, where information from forward detectors is additionally included. This format is created by selecting the necessary information from MuDst format data files containing outputs from all available STAR detectors and information on reconstructed trajectories of produced particle. The standard MuDst files are unsuitable for specific analysis because of their sizes exceeding 600 TB. The picoDst files are up to 100 times smaller.

A smaller sample of the data was available to me locally on my computer so that it is possible to check the functionality of the written program. The full analysis then means applying the program to data from Run17 available from the STAR database through a remote access using a SDCC BNL account. Specifically, it is 2261 ROOT files and the result of the analysis is one merged ROOT file containing the information from all individual files at once. The typical runtime of this full analysis is in the unit of hours.

Traditional framework used for the analysis of particle collision data is the program ROOT [27]; an object-oriented program and library developed by CERN. My work was based on a C++ program that I used for by analysis for my bachelor thesis. I gradually added the parts needed for my analysis to this macro and made changes so that is fits to this specific analysis. Mainly the work was about the implementation of selection rules (cuts) for events, defining the necessary distributions to check the steps of the analysis and investigate the distributions of the wanted results such as the invariant mass and missing p_{T}.

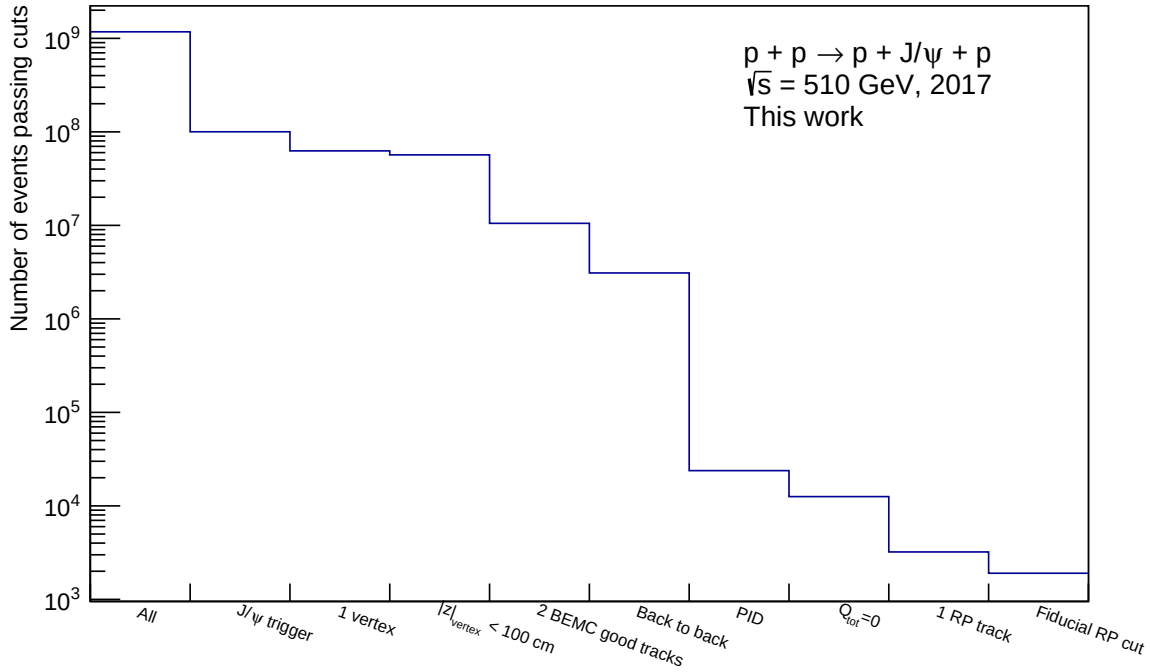

Figure 3.7: Histogram showing the reducing of the number events passing selection criteria in each step.

In my analysis, I start by selecting only the events from the dataset that are fit for further analysis. That is done by applying selection criteria/cuts on events and the particle tracks they contain. The step-by-step selection is represented in Fig. 3.7, where the histogram shows the number of events satisfying the criteria in each step starting with the full number of events in the dataset and ending with the cuts regarding the forward-proton tracks. My specific cuts and their reasoning are the following (numbering corresponds to columns in the cuts flow histogram):

2) **J/ψ trigger**: First I only allow the events that are selected by the J/ψ trigger called JPsi*HTTP. This cut leaves 100.22 million events.

3) **1 vertex**: Only events with exactly one vertex with a track with a BEMC hit are allowed to rule out pile-up events from other collisions.

4) $|z|_{\mathbf{vertex}} < 100$ **cm**: Maximal distance of the primary vertex from the centre of the TPC must be 100 cm to ensure the track coming out of it are in a high-geometrical-acceptance region of the BEMC detector.

5) **2 BEMC good tracks**: This cut defines good quality tracks and only allows events containing exactly two. Step by step selection of tracks is shown in Fig. 3.8 which includes the number of tracks satisfying each criteria. The used cuts are the following

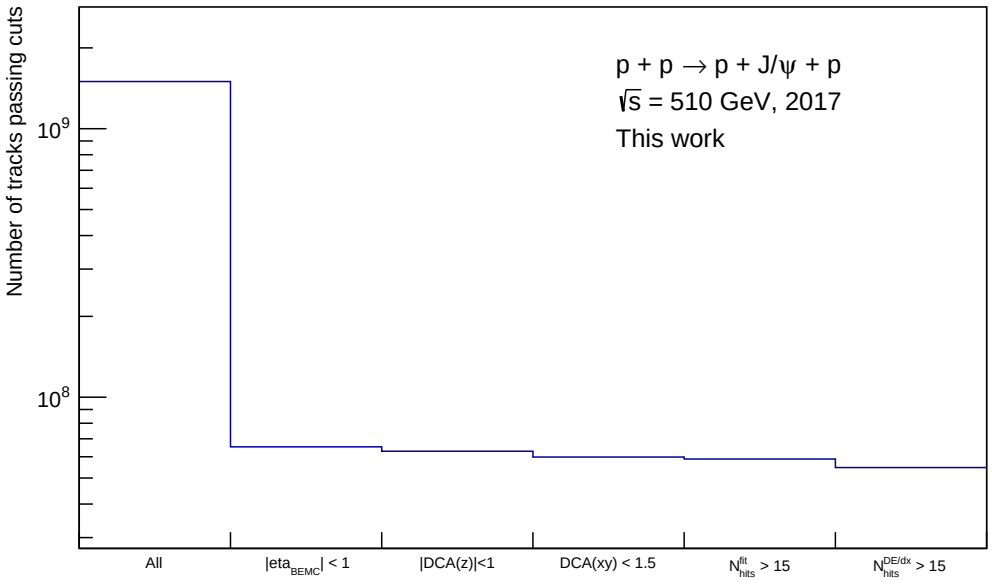

Figure 3.8: Histogram showing the reducing of the tracks events passing selection criteria in each step.

- $|\eta_{\mathbf{BEMC}}| < 1$: The maximum allowed value of track pseudorapidity as measured in BEMC is set to one to ensure they are in a region of good BEMC acceptance.
- $|\mathbf{DCA}_z| < 1$ **cm and** $\mathbf{DCA}_{xy} < 1.5$ **cm**: Maximum allowed distance of closes approach in the z-axis is 1 cm and in the transversal plane xy 1.5 cm to make sure both tracks begin in the one primary vertex.
- $N^{\mathbf{fit}}_{\mathbf{hits}} > 15$ **and** $N^{\mathbf{d}E/\mathbf{dx}}_{\mathbf{hits}} > 15$: Minimal number of hits in TPC used to reconstruct the track trajectory is 15, and minimal number of points used to calculate the energy loss is 15. Important quantities for further analysis such as momentum are calculated based on the curvature of the track so it is important to have accuracy of the track fit.

- **2 tracks**: Chose only events with exactly two tracks in with BEMC hits as the studied process is expected to produce two daughter particles. If two or more such tracks were allowed, it would be necessary to deal with looking through various combinations to find one right pair for which a peak corresponding to J/ψ is observable in the data. This approach might be used later in the analysis.

6) **Back-to-back**: The two chosen tracks have to be back-to-back based on their hits in BEMC to confirm the condition as it is done in the trigger. It is done by segmenting the full azimuthal angle of BEMC into six sections. Each track is assigned a segment numbed based on its hit position. The cuts requires the segments of the two tracks to be opposite each other as represented in Fig. 3.9.

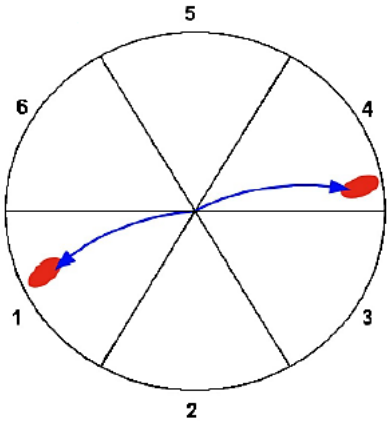

Figure 3.9: Diagram of BEMC segments as used to check for back-to-back tracks.

7) **PID**: Particle identification is done based on the measured energy loss in the TPC of the particle and its momentum. The quantity of $n\sigma$ is calculated as $n\sigma_{\text{particle}} = \ln\left(\frac{\mathrm{d}E/\mathrm{d}x}{\mathrm{d}E/\mathrm{d}x|_{\text{expected}}}\right)/\sigma_{\text{TPC}}$, where $\mathrm{d}E/\mathrm{d}x$ is the measured energy loss, $\mathrm{d}E/\,\mathrm{d}x|_{\text{expected}}$ is the expected energy loss according to the parametrization of the Bethe-Bloch formula, and σ_{TPC} is the TPC resolution. This means the smaller the $n\sigma$ value the more certain we can be in a proper identification. Electrons and positrons are selected by requiring $\chi^2_{\text{ee}} = \text{n}\sigma^2_{\text{e}} + \text{n}\sigma^2_{\text{e}} < 3^2$. Possible background from Kaons, pions and protons is rejected by cuts $\chi^2_{\text{KK}} > 10$, $\chi^2_{\pi\pi} > 10$ and $\chi^2_{\text{pp}} > 10$.

8) $Q_{\text{tot}} = 0$: As the studied decay channel final-state particles are an electron and a positron, which have opposite charge, the total charge of the two tracks in the event is required to be zero.

9) **1 RP track**: Exactly one proton must detected in the event by both RP stations either in east or west direction. At least ¾ planes in each RP station must measure it.

10) **Fiducial RP cut**: For securing a high track reconstruction efficiency it is required for the detected protons to fall into a region of high acceptance of RP; the fiducial region. The momentum plane with the fiducial region bordered

by the red curve is shown in Fig. 3.10. The cut only allows the events with protons inside this region, which is defined as:

$(p_x + 0.6\ \text{GeV}/c)^2 + {p_y}^2 < 1.25\ \text{GeV}^2/c^2$

$0.4\ \text{GeV}/c < |p_y| < 0.8\ \text{GeV}/c$

$p_x > -0.27\ \text{GeV}/c$

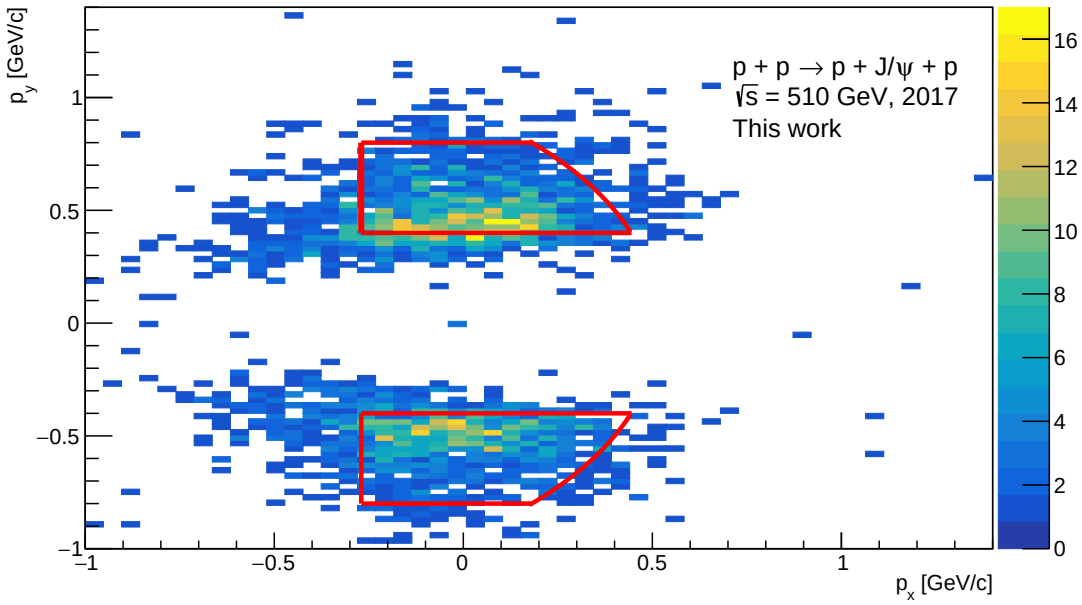

Figure 3.10: A 2D histogram showing the fiducial cut on RP track momentum. Red dashed lines represent the limit values used, where the selected events are bordered by them.

The last two are cuts regarding the forward proton detected in Roman Pots. The Roman Pot detector system gives the unique opportunity to divide the analysis in two ways. The order of the selection criteria is such that, after examining the trigger and vertex properties, the quality of the tracks in the central barred is examined first, followed by cuts pertaining to the quality of tracks in Roman Pots. The results of this analysis are separated and presented as either "before RP cuts" or "after RP cuts".

Chapter 4

Discussion of the Results

The total number of events passing the cuts is 12565 before RP cuts and 1904 after RP cuts. These events are used to see the following results.

4.1 Invariant Mass and Raw Yield

The first result presented is the uncorrected invariant mass of electron-positron pairs. In particle physics, the invariant mass is equal to the mass in the rest frame of the particle. In the process of the analysis it is calculated using the daughters particles' energy E and momentum p which are stored for the tracks, by the energy–momentum relation $m_{ee} = \sqrt{(E_1 + E_2)^2 - (\overrightarrow{p_1} + \overrightarrow{p_2})^2}$.

The uncorrected invariant mass of the electron-positron pairs is shown in Fig. 4.1 and 4.2 for events before and after RP curs respectively. In black is the unlike-sign distribution and in red the background of like-sign distribution. Distribution is shown starting at 2 GeV/c^2 as the trigger is inefficient below this value and the distribution does not interest us. The J/ψ peak is prominent for both distributions.

The like-sign background was subtracted to get the distributions in Fig. 4.3 and 4.4. For both plots the fitting of the data was done the same way. Data in the peak region were fitted with a composite function (Gaussian + second polynomial) depicted in green colour on the plots. The background was then estimated using the same second polynomial function, which is depicted in red on the plots.

The J/ψ mass resulting from the fit of the "before RP cuts" distribution is $m_{J/\psi} = 3.08 \pm 0.05$ GeV/c^2. And the same for the "after RP cuts" distribution is $m_{J/\psi} = 3.085 \pm 0.006$ GeV/c^2. These results are in the form of centre-of-Gaussian parameter ± width-of-Gaussian parameter. These masses found in this work are comparable with the reference value from Particle Data Booklet $m_{\mathrm{PDG}} = 3096.900 \pm$ 0.006 MeV/c^2 [28].

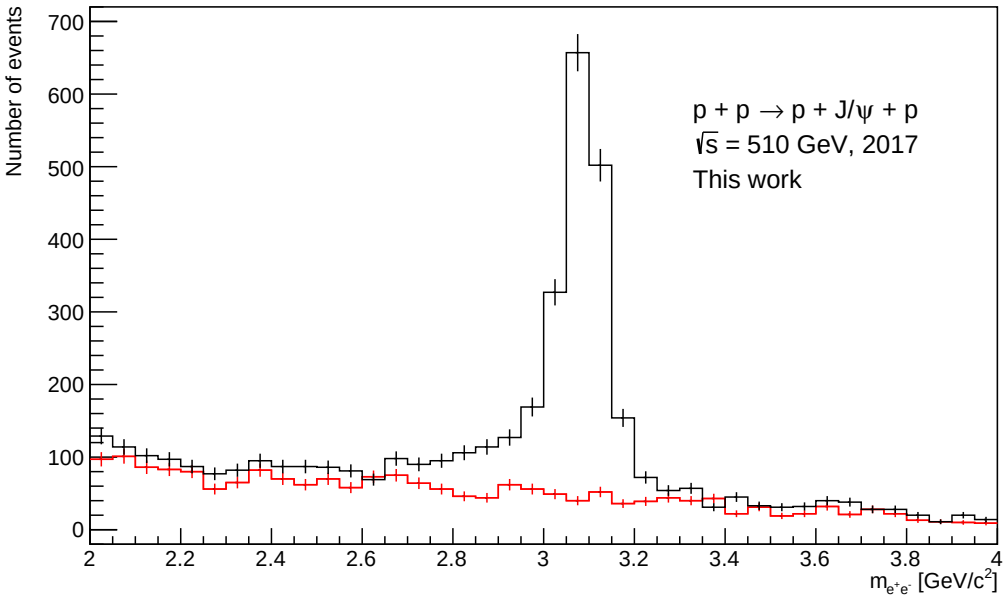

Figure 4.1: Uncorrected invariant mass distribution of electron-positron pairs for events before the RP cuts are applied. Unlike-sign in black and like-sign in red.

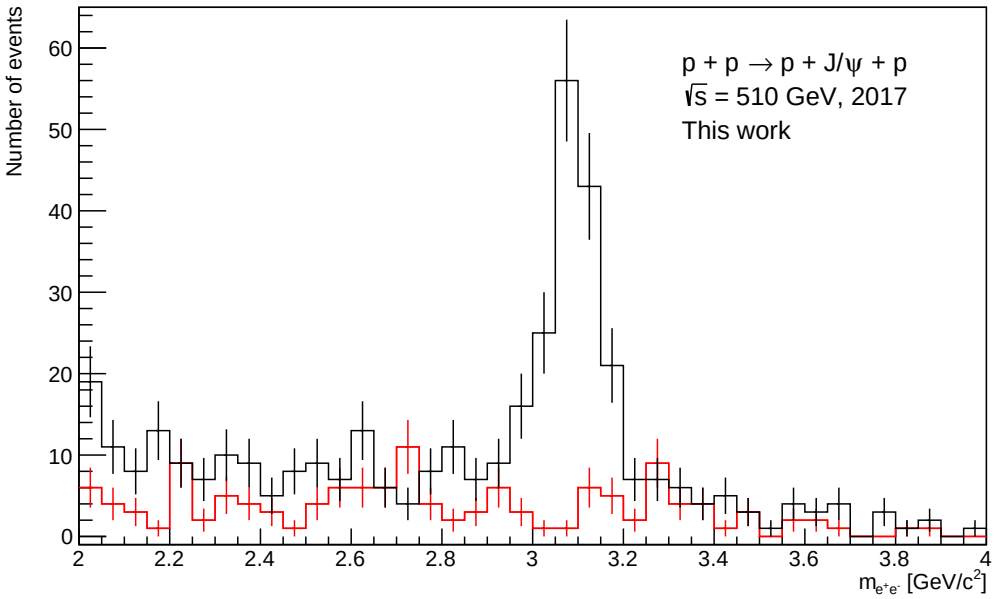

Figure 4.2: Uncorrected invariant mass distribution of electron-positron pairs for events after the RP cuts are applied. Unlike-sign in black and like-sign in red.

From the fit results the raw yield was calculated subtracting the integral of the background function from the integral of the signal function in the mass region of $m_{J/\psi} \pm 3\sigma$ depicted by the dashed black lines in the plots. After including the correction for bin size (50 GeV/c^2) into the calculation the raw yields are 1534 with the signal significance of $S/B = 27$ "before RP cuts" and 137 "after RP cuts" with the signal significance of $S/B = 15$.

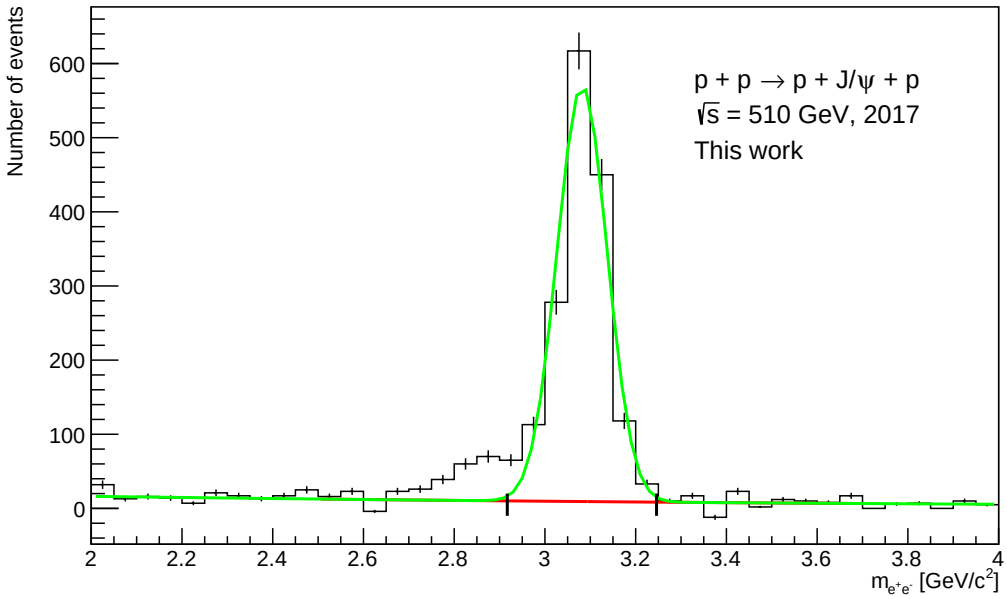

Figure 4.3: Fit of uncorrected invariant mass distribution of electron-positron pairs for events before the RP cuts are applied after the subtraction of like-sign distribution. Fit of data in peak region by green function (Gauss + second polynomial), background estimated by red function (second polynomial).

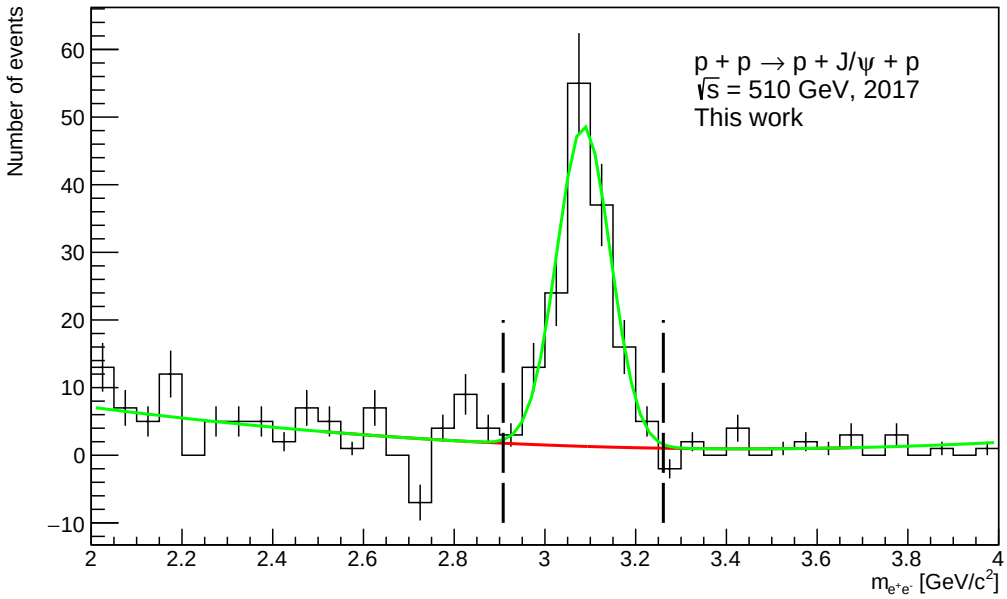

Figure 4.4: Fit of uncorrected invariant mass distribution of electron-positron pairs for events after the RP cuts are applied after the subtraction of like-sign distribution. Fit of data in peak region by green function (Gauss + second polynomial), background estimated by red function (second polynomial).

4.2 Balance Between J/ψ and Forward Proton

It is in the interest of this analysis to check the balance between the forward proton and the reconstructed J/ψ in the central barrel. Hence we look for the balance in the azimuthal angle and transverse momentum. All plots in this section are done for events after RP cuts and only for mass-candidates of J/ψ ($\pm 3\sigma$ region based on fit result).

AZIMUTHAL ANGLE

The detected proton and reconstructed J/ψ should be back-to-back based on the kinematics of the collision. This is checked two ways. Firstly by looking at the distribution of the absolute value of the difference of azimuthal angles of the proton and J/ψ denoted as $\Delta\phi = |\phi_p - \phi_{J/\psi}|$. If they are indeed back-to-back this difference should be π.

This distribution is shown in Fig. 4.5 with the unlike-sign events in black and the background of like-sign events in red. In Fig. 4.2 is the distribution after the like-sign background is subtracted. The peak sits at the expected value proving the two particles to be back-to-back.

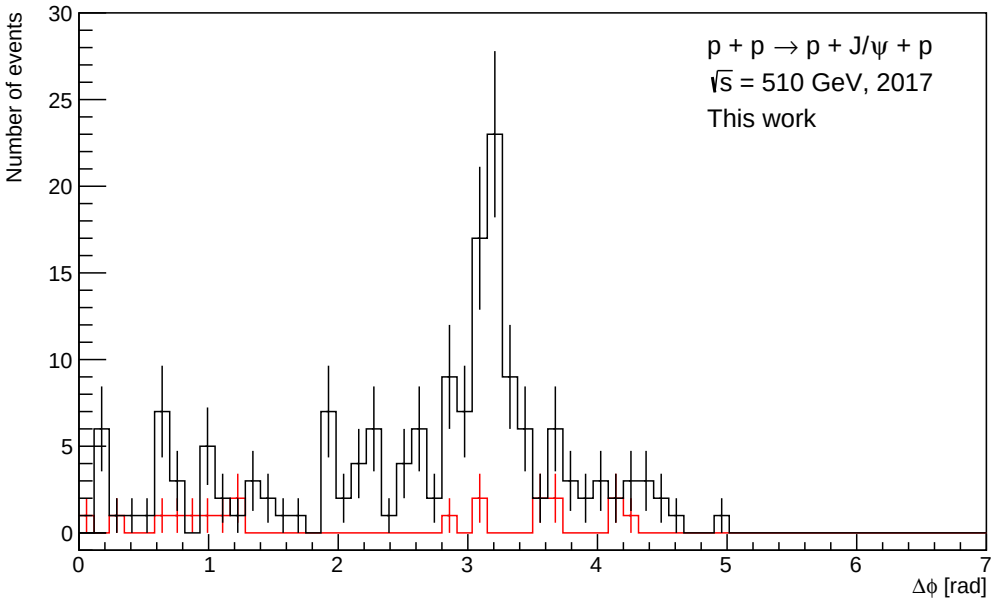

Figure 4.5: Distributions of the absolute value of the difference of the azimuthal angle of proton and J/ψ ($\Delta\phi$). Unlike-sign in black and like-sign in red.

The second way of checking is to look for correlation in a 2D plot of the two azimuthal angle. For back-to-back particles the events would sit on a diagonal line. This plot and the correlation line is shown in Fig. 4.7. Even though the statistics in this analysis is not high the correlation still can be seen.

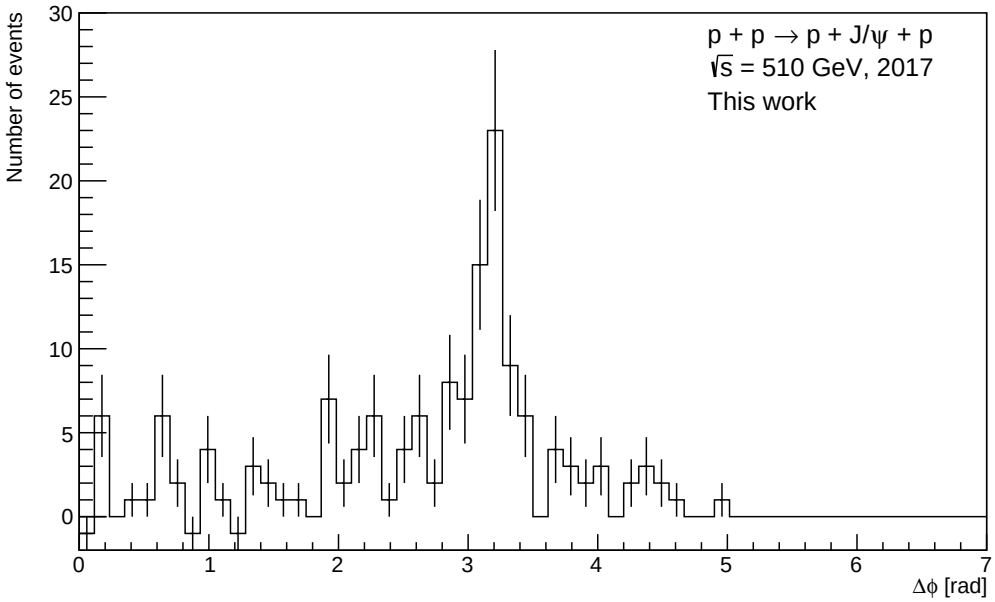

Figure 4.6: Distribution of the absolute value of the difference of the azimuthal angle of proton and J/ψ ($\Delta\phi$) after subtraction of like-sign background.

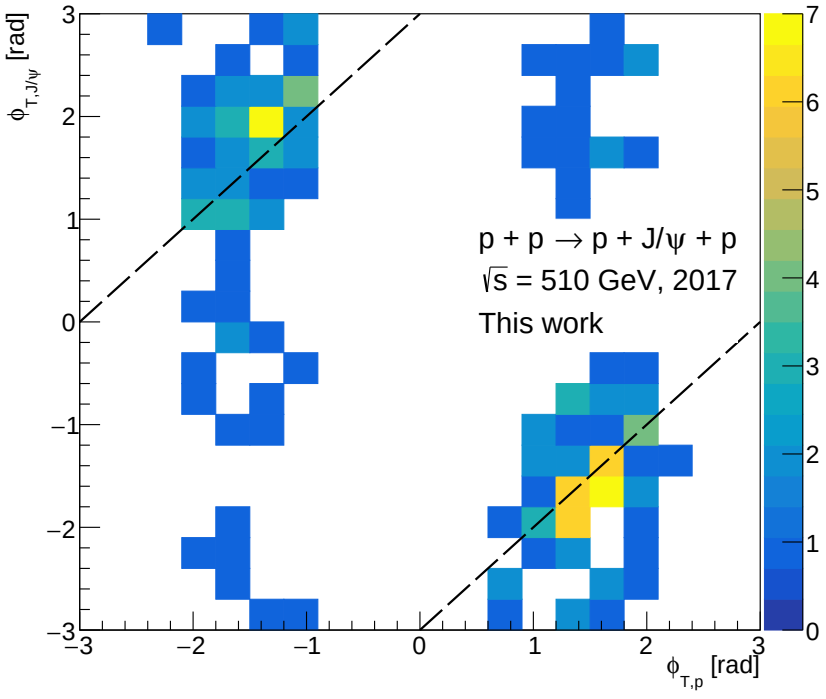

Figure 4.7: A 2D distribution of azimuthal angle of proton and J/ψ with expected correlation symbolised by a line.

TRANSVERSE MOMENTA

This balance comes from the conservation of transverse momentum in the interaction, which states: $\left(\boldsymbol{p}_1 + \boldsymbol{p}_2 + \boldsymbol{p}_{\mathrm{J}/\psi}\right)_{\mathrm{T}} = 0$. The small-$p_{\mathrm{T}}$ proton (proton 2) scatters at a small angle, hence the p_{T} of the virtual photon is small. We take $p_{1,\mathrm{T}} \sim 0$ which gives $\boldsymbol{p}_{2,\mathrm{T}} = -\boldsymbol{p}_{\mathrm{J}/\psi}$.

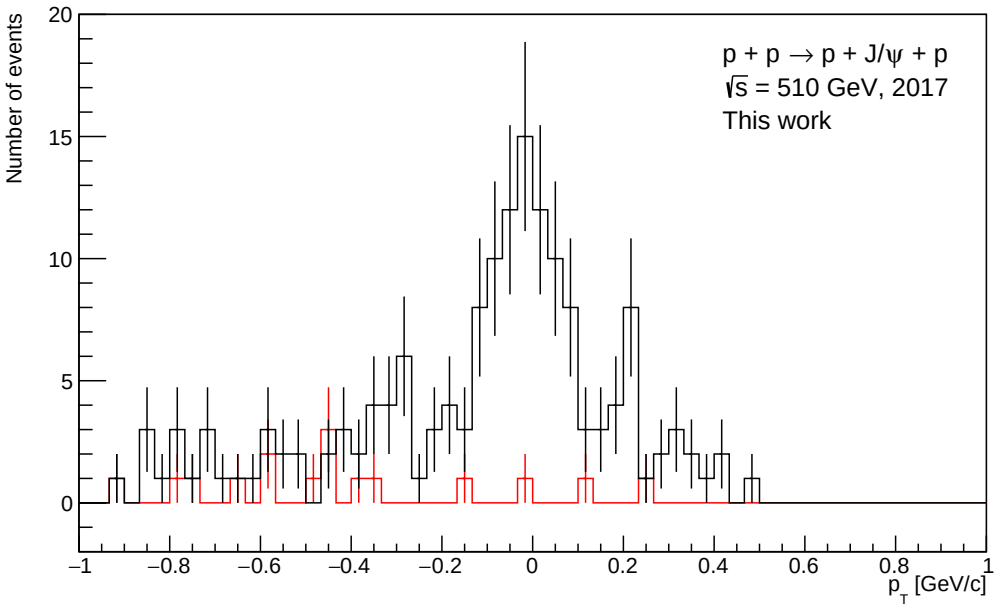

Figure 4.8: Distributions of the absolute value of the difference of the transverse momenta of proton and J/ψ ($|\boldsymbol{p}_{2,\mathrm{T}} - \boldsymbol{p}_{\mathrm{J}/\psi}|$). Unlike-sign in black and like-sign in red.

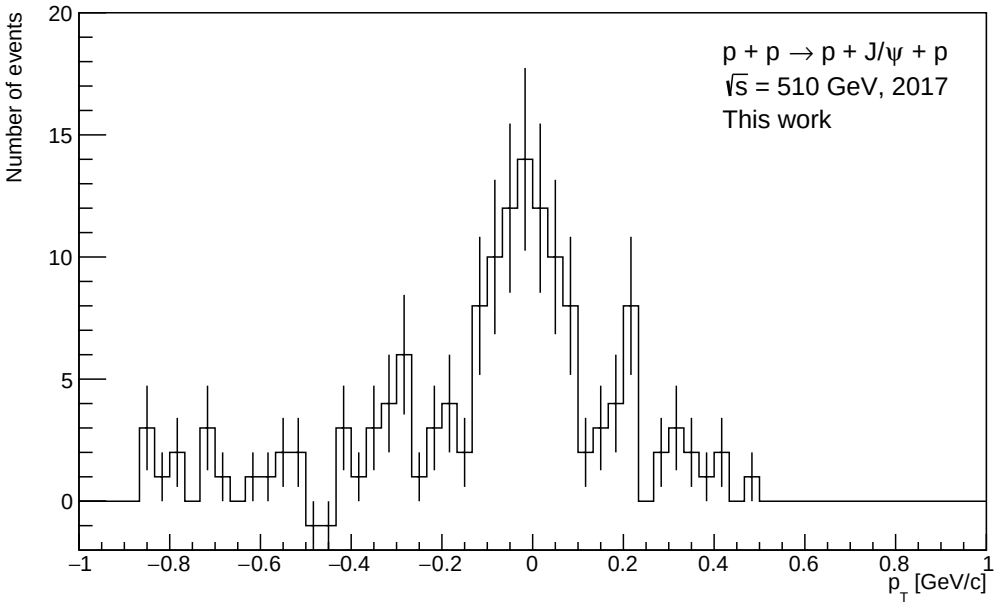

Figure 4.9: Distribution of the absolute value of the difference of the transverse momenta of proton and J/ψ ($|\boldsymbol{p}_{2,\mathrm{T}} - \boldsymbol{p}_{\mathrm{J}/\psi}|$) after subtraction of like-sign background.

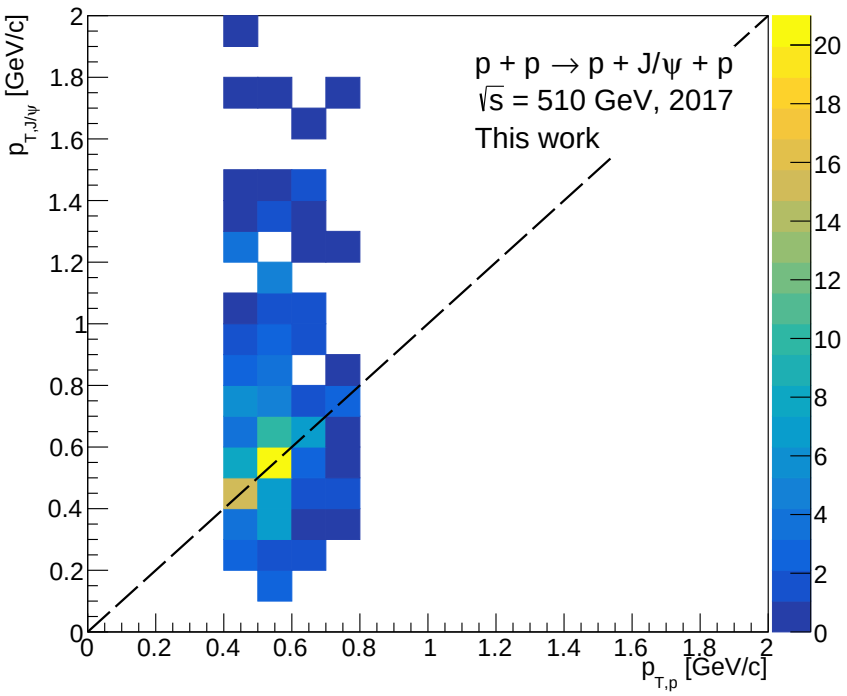

Figure 4.10: A 2D distribution of transverse momenta of proton and J/ψ with expected correlation symbolised by a line.

This fact is again checked two ways. First by looking at the distribution of the difference $|\boldsymbol{p}_{2,\mathrm{T}} - \boldsymbol{p}_{\mathrm{J}/\psi}|$ as can be seen in Fig. 4.8 with the unlike-sign events in black and the background of like-sign events in red. In Fig. 4.9 is the distribution other the like-sign background is subtracted. The peak sits at around zero as expected from the balance prerequisites.

The second way is looking for correlation in a 2D plot of the two transverse momenta. For particles balancing each other the events should sit on a diagonal line. This is depicted in Fig. 4.10 where again despite the small statistics the correlation is visible.

4.3 Missing p_{T}

As was already mentioned before, this analysis might pose an unique opportunity to get a precise measurement of transverse momenta of the virtual photon in this photoproduction interaction. The value of this quantity is expected to be quite small, hence it is difficult to measure considering detector resolutions and efficiencies. To recall the equation to calculate this so-called missing p_{T} is: $-\boldsymbol{p}_{2,T} = \left(\boldsymbol{p}_1 + \boldsymbol{p}_{\mathrm{J}/\psi}\right)_{\mathrm{T}}$, where p_1 is momenta of the Pomeron-side proton measured in Roman Pots and $p_{\mathrm{J}/\psi}$ is momenta of J/ψ reconstructed from the detected electron and positron pairs.

Distribution of missing p_{T} after the subtraction of like-sign background is shown in Fig. 4.11. What we see is one narrow peak near zero in the section labelled "A" which corresponds to the exclusive studied process. In the section labelled "B" starting at around 0.3 GeV/c there is a second wide peak containing the non-exclusive background contamination. The offset of the first peak from zero is caused by the Jacobian of the transformation when calculating the transverse momentum.

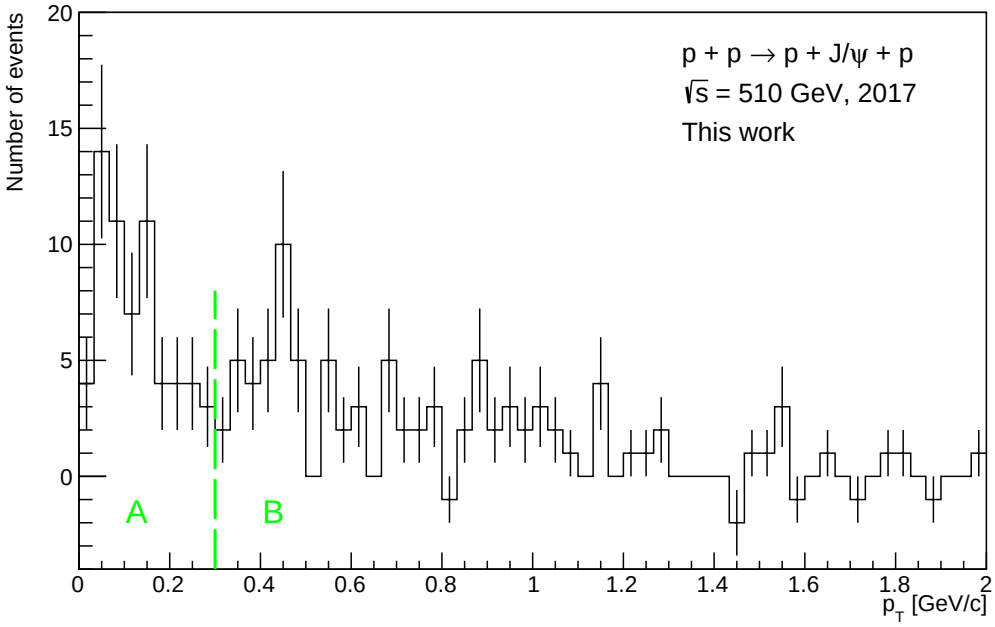

Figure 4.11: Distribution of the missing p_{T} which represents the transverse momenta of the virtual photon in the interaction after subtraction of like-sign background. Data in section labelled "A" is expected to correspond to the exclusive studied process and in the section labelled "B" starting at around 0.3 GeV/c there is a second wide peak containing the non-exclusive background contamination.

The shape of the distribution is comparable to previous measurements of missing p_{T}. This resemblance is shown by comparing the obtained distribution of missing p_{T} with unlike-sign distribution in black and the background of like-sign distribution in red from this work on Fig. 4.12. On Fig. 4.13 is missing p_{T} of the system $p + \pi + \pi + p$ from the measurement of central exclusive production at the STAR experiment in pp collisions at $\sqrt{s} = 200$ GeV in 2015 [29]. The expected shape can be seen on the distribution from this work despite the much smaller statistics.

To get the virtual photon p_{T} those two peaks need to be fitted to extract just the events belonging to the first peak. The RP and J/ψ resolutions, which are expected to be a few tens MeV, need to be incorporated. The small statistics and not-good-enough resolution might prevent obtaining the exact value of the photon p_{T}. In that case, this analysis will at least present an upper limit on this number.

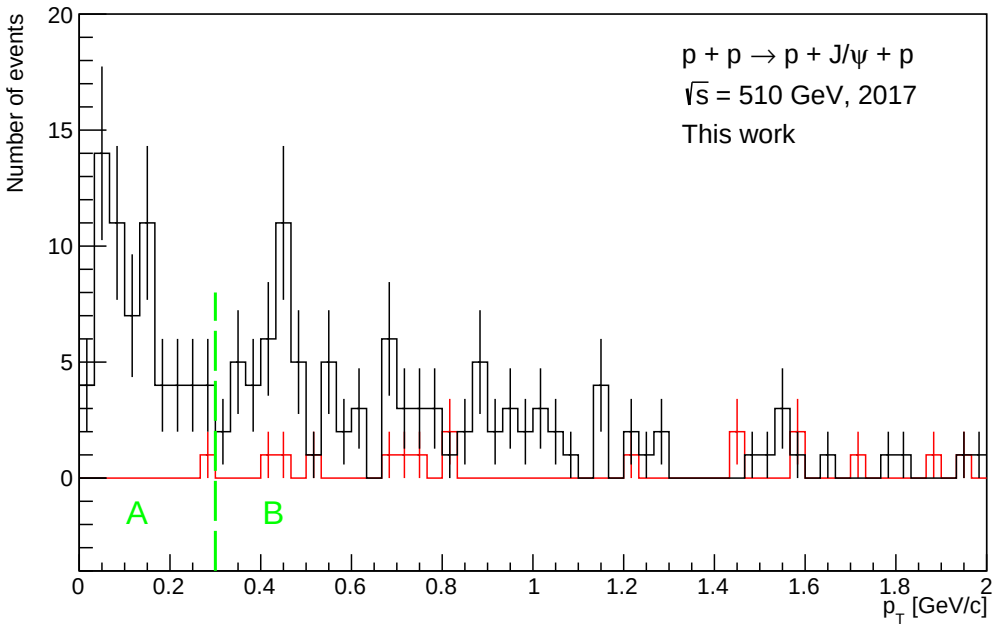

Figure 4.12: Distributions of the missing p_{T} which represents the transverse momenta of the virtual photon in the interaction. Unlike-sign in black and like-sign in red.

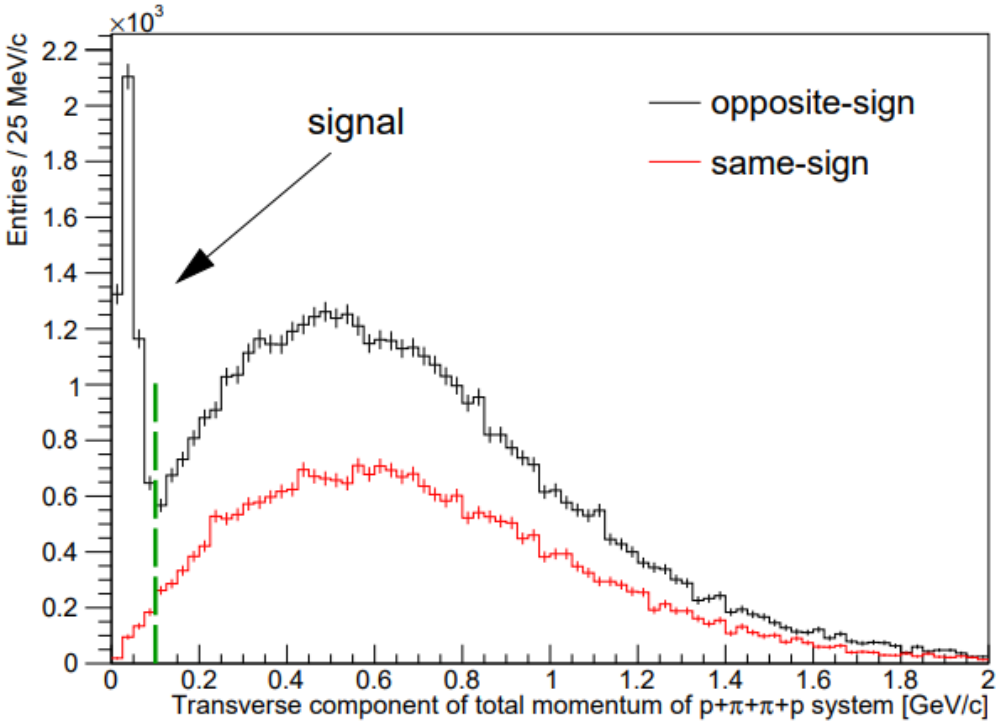

Figure 4.13: Missing p_{T} from a comparable measurement of central exclusive production at the STAR experiment in pp collisions at $\sqrt{s} = 200$ GeV in 2015. Taken from Ref. [29].

Conclusion

In this thesis, the theory pertinent to photoproduction processes was presented, focusing particularly on J/ψ photoproduction in proton-proton collisions. The work began by demonstrating the parallels between fundamental theory of hadronic diffraction and classical optics. Subsequently, the kinematics of diffractive processes were reviewed, followed by Regge Theory's introduction across different energy scales. Then the thesis moved to the concept of ultraperipheral collisions and the unique insights they offer into hadronic structure. The examination of J/ψ photoproduction followed, which involves the creation of particles through photon-nucleon interactions, yielding valuable insights into quantum chromodynamics and nucleon structure. The findings from experiments conducted by ALICE and STAR experiment were shown to discuss our understanding of the topic.

The subsequent discussion provided an overview of the results of my data analysis work. This project aimed to start with the analysis of the J/ψ photoproduction in pp collisions at $\sqrt{s} = 510$ GeV measured by the STAR experiment in 2017 and investigate the possibility of precise measurement of the transverse momenta of the virtual photon present in the process.

The J/ψ vector meson is reconstructed through the decay channel into the electron-positron pairs. In this analysis, I utilized the Time Projection Chamber and Barrel Electromagnetic Calorimeter detectors to identify the electron and positron tracks. For the detection of the forward proton, I used the Beam Beam Counter and Roman Pot detectors. I started by implementing the selection criteria to get a clean set of events for further analysis into the analysis code. The cuts revolve around the properties of the vertices and tracks in the central barrel of the STAR experiment as well as of the forward protons in Roman Pots. I found that the additional cuts regarding the protons lower the statistics approximately by ten. These cuts have to be fine-tuned to be strict enough to ensure the quality of the chosen events and tracks but not too harsh due to quite small statistics.

Using the selected data set, I identified the J/ψ vector meson in the uncorrected invariant mass distribution of the electron-positron pairs. I subtracted the combinatorial background consisting of electron-electron and positron-positron pairs from it. This result can be seen on Fig. 4.3 and Fig. 4.4. The calculated raw yield before and after the Roman Pot cuts are applied is 1534 and 137 vector mesons respectively.

I checked the balance between the forward proton and the reconstructed J/ψ in azimuthal angle and transverse momenta to verify the conservation of momentum in the collision. This can be seen at plots on Fig. 4.6 and Fig. 4.9.

The main interest of this analysis was the first look at the missing p_{T} of the virtual photon present in the process. The distribution of this variable is on Fig. 4.11 and Fig. 4.12. The shape of the distribution is compared to a previous similar mea-

surement shown on Fig. 4.13. Both expected peaks, the narrow peak near zero that corresponds to the studied process and the subsequent wide peak starting around 0.3 GeV/c containing the non-exclusive background contamination, are seen in the obtained distribution. As was discussed we will see if the precise measurement of the photon transverse momentum is possible when the detector resolutions are incorporated by continuing investigation of this problem.

Apart from the photon p_{T} the other final result this analysis is working towards is the cross-section of the J/ψ photoproduction as a function of the transferred momenta, $-t$. For this the corrected invariant mass distribution needs to be obtained. For this, I am currently working on generating events by Starlight event generator. In this process, I am learning to work with the Starlight program and its configuration.

Bibliography

1. BARONE, V.; PREDAZZI, E. *High-energy particle diffraction*. Springer Science & Business Media, 2002.
2. PARTICLE DATA GROUP. 20. High Energy Soft QCD and Diffraction; Review of particle physics. *PTEP*. 2020, vol. 2020, no. 8, pp. 1–2093.
3. KLEIN, S.; NYSTRAND, J. Ultraperipheral nuclear collisions. *Phys. Today*. 2017, vol. 70, no. 10, pp. 40–47. ISSN 0031-9228.
4. ALDEBARAN. Částice a interakce, Standardní model. 2022. Available also from: `https://www.aldebaran.cz/astrofyzika/interakce/standardmodel.php`.
5. AAD, G. et al. Observation of a new particle in the search for the Standard Model Higgs boson with the ATLAS detector at the LHC. *Phys. Lett. B*. 2012, vol. 716, no. 1, pp. 1–29.
6. MUELLER, A. H. *Parton Saturation-An Overview*. 2001. Available from arXiv: `hep-ph/0111244 [hep-ph]`.
7. ABRAMOWICZ, H.; CALDWELL, A. HERA collider physics. *Rev. Mod. Phys.* 1999, vol. 71. Available from arXiv: `hep-ex/9903037`.
8. GOOD, M. L.; WALKER, W. D. Diffraction Dissociation of Beam Particles. *Phys. Rev.* 1960, vol. 120, pp. 1857–1860.
9. BJORKEN, J. D. *Hard diffraction and deep inelastic scattering*. 1994. Tech. rep. Stanford Linear Accelerator Center.
10. DERRICK, M. et al. Observation of events with a large rapidity gap in deep inelastic scattering at HERA. *Phys. Lett. B*. 1993, vol. 315, no. 3, pp. 481–493. ISSN 0370-2693. Available also from: `https://www.sciencedirect.com/science/article/pii/0370269393916454`.
11. BECKER, F. M. *Far Field, Fraunhofer Diffraction Patterns*. Available also from: `https://users.ece.utexas.edu/~becker/diffract.pdf`.
12. CHEW, G. F. *S*-Matrix Theory of Strong Interactions without Elementary Particles. *Rev. Mod. Phys.* 1962, vol. 34, pp. 394–401.
13. *Feynman and Regge Poles*. Available also from: `https://ysfine.com/feynman/chewfrau.html`.
14. ABELEV, B. et al. Exclusive J/ψ Photoproduction off Protons in Ultraperipheral p-Pb Collisions at $\sqrt{s_{\mathrm{NN}}} = 5.02$ TeV. *Phys. Rev. Lett.* 2014, vol. 113, p. 232504.
15. ADLER, C. et al. Coherent ρ^0 Production in Ultraperipheral Heavy-Ion Collisions. *Phys. Rev. Lett.* 2002, vol. 89, p. 272302.

16. ACHARYA, S. et al. Energy dependence of exclusive J/ψ photoproduction off protons in ultra-peripheral $p - Pb$ collisions at $\sqrt{s_{\mathrm{NN}}} = 5.02$ TeV. *Eur. Phys. J. C., Particles and Fields*. 2019, vol. 79, no. 5, pp. 1–18.

17. ABDALLAH, M. S. et al. Probing the Gluonic Structure of the Deuteron with J/ψ Photoproduction in d + Au Ultraperipheral Collisions. *Phys. Rev. Lett.* 2022, vol. 128, p. 122303.

18. ACKERMANN, K. H. et al. STAR detector overview. *Nucl. Instrum. Methods. Phys. Res. A: Accelerators, Spectrometers, Detectors and Associated Equipment*. 2003, vol. 499, no. 2-3, pp. 624–632.

19. *RHIC accelerator website*. Available also from: `https://www.bnl.gov/rhic/`.

20. *Brookhaven National Laboratory website*. Available also from: `https://www.bnl.gov/`.

21. BÜLTMANN, S. et al. The PP2PP experiment at RHIC: silicon detectors installed in Roman Pots for forward proton detection close to the beam. *Nucl. Instrum. Methods. Phys. Res. A:: Accelerators, Spectrometers, Detectors and Associated Equipment*. 2004, vol. 535, no. 1-2, pp. 415–420.

22. GURYN, W.; PAWLIK, B. Results on Total and Elastic Cross Sections in Proton-Proton Collisions at $\sqrt{s} = 200$ GeV Obtained with the STAR Detector at RHIC. 2020. Available from arXiv: `2005.00776 [hep-ex]`.

23. ANDERSON, M. et al. The STAR time projection chamber: a unique tool for studying high multiplicity events at RHIC. *Nucl. Instrum. Methods. Phys. Res. A: Accelerators, Spectrometers, Detectors and Associated Equipment*. 2003, vol. 499, no. 2-3, pp. 659–678.

24. STAR COLLABORATION. The Beam-Beam Counter: A Local Polarimeter at STAR. In: *AIP Conference Proceedings*. American Institute of Physics, 2008, vol. 980, pp. 390–396. No. 1.

25. BEDDO, M. et al. The STAR barrel electromagnetic calorimeter. *Nucl. Instrum. Methods. Phys. Res. A: Accelerators, Spectrometers, Detectors and Associated Equipment*. 2003, vol. 499, no. 2-3, pp. 725–739.

26. ADAMCZYK, L. et al. Single spin asymmetry AN in polarized proton-proton elastic scattering at $\sqrt{s} = 200$ GeV. *Phys. Lett. B*. 2013, vol. 719, no. 1-3, pp. 62–69.

27. RADEMAKERS, F. et al. Root status and future developments. *arXiv preprint cs/0306078*. 2003.

28. PARTICLE DATA GROUP. Review of particle physics. *PTEP*. 2020, vol. 2020, no. 8, p. 083C01.

29. SIKORA, R. Central exclusive production in the STAR experiment at RHIC. In: *AIP Conference Proceedings*. AIP Publishing LLC, 2017, vol. 1819, p. 040012. No. 1.

Appendix

A Event selection plots

For the sake of readability the plots of all individual cuts used in my data analysis were not included in the main text of the chapter 3.2, but are rather displayed here. The complete set of cuts and their reasoning is explained in the chapter 3.2. Following is a short summary of these cuts. The cuts are presented in chronological order as they are used in the analysis with the corresponding plots linked in brackets. Red dashed lines represent the limit values used.

The analysis focused on JPsi*HTTP trigger events with a total count of 100.22 million. Criteria were set to include only events with exactly one vertex, ensuring the vertex $|z|$ position was below 100 cm (Fig. 14).

Primary track selection required pseudorapidity of primary tracks as detected by the BEMC detector to be less than one (Fig. 15); the distance of closest approach in z-axis is required to be below 1 cm (Fig. 16) and in the xy plane less than 1.5 cm (Fig. 17); the number of point recorded in the TPC used to reconstruct the track must be greater than 15 (Fig. 18) and the number of point from which the energy loss for the tracks is calculated must be greater than 15 (Fig. 19). Events with exactly two tracks originating from the primary vertex, each possessing BEMC hits, were considered.

Back-to-back tracks were identified in BEMC and selected (Fig. 20). The two tracks were identified as electron or positron through on the particle identification based on energy loss (Fig. 21) and cuts were applied to remove possible proton, Kaon and pion background.

The total transverse momentum of the two identified particles was set to zero, allowing for the separation of unlike-signed and like-signed tracks.

Followed a requirement involved having exactly one good track in the Roman Pot detectors (Fig. 22). Finally, tracks in the RP were confined to the fiducial region for further analysis (Fig. 23).

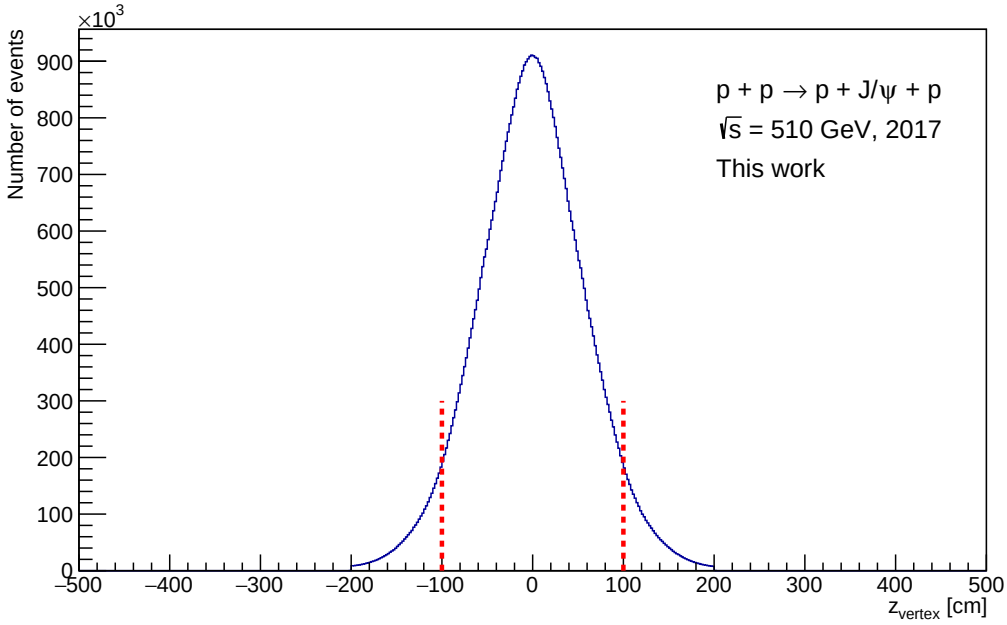

Figure 14: Histogram showing the vertex position cut. Red dashed lines represent the limit values used, where the selected events are in between.

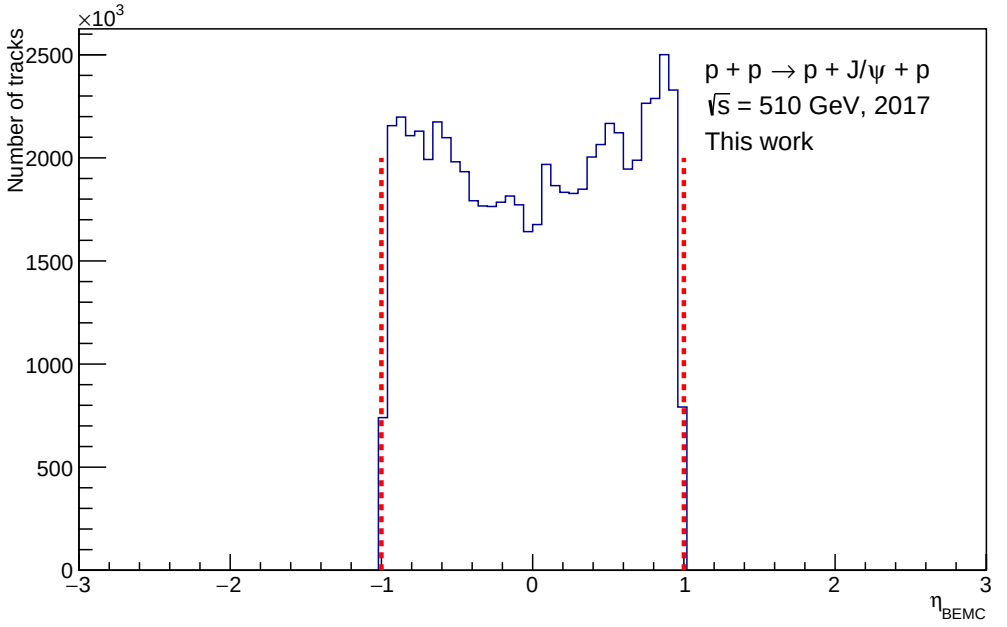

Figure 15: Histogram showing the pseudorapidity cut. Red dashed lines represent the limit values used, where the selected events are in between.

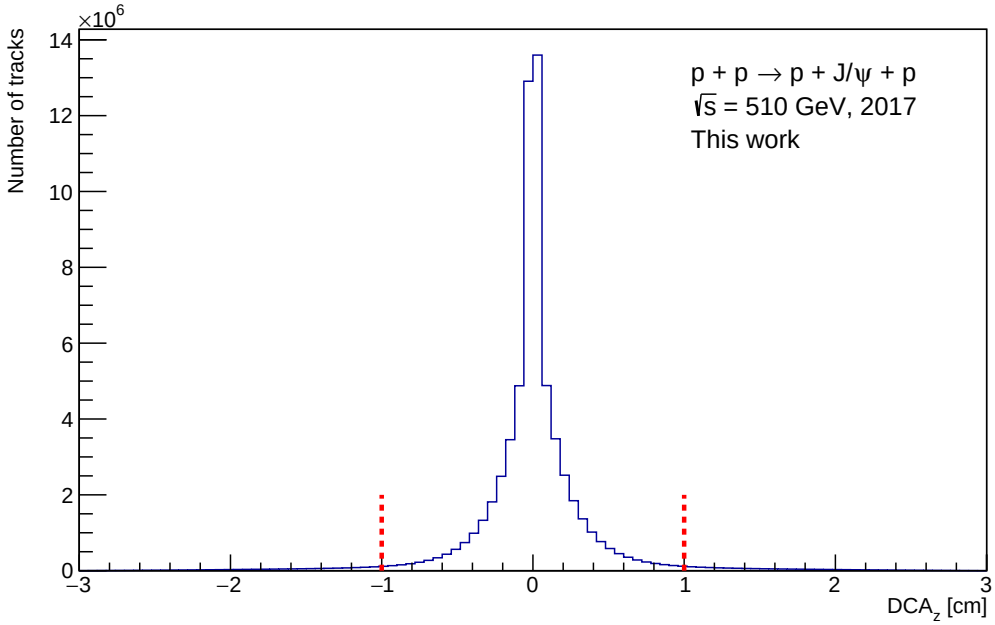

Figure 16: Histogram showing the DCA cut in z axis. Red dashed lines represent the limit values used, where the selected events are in between.

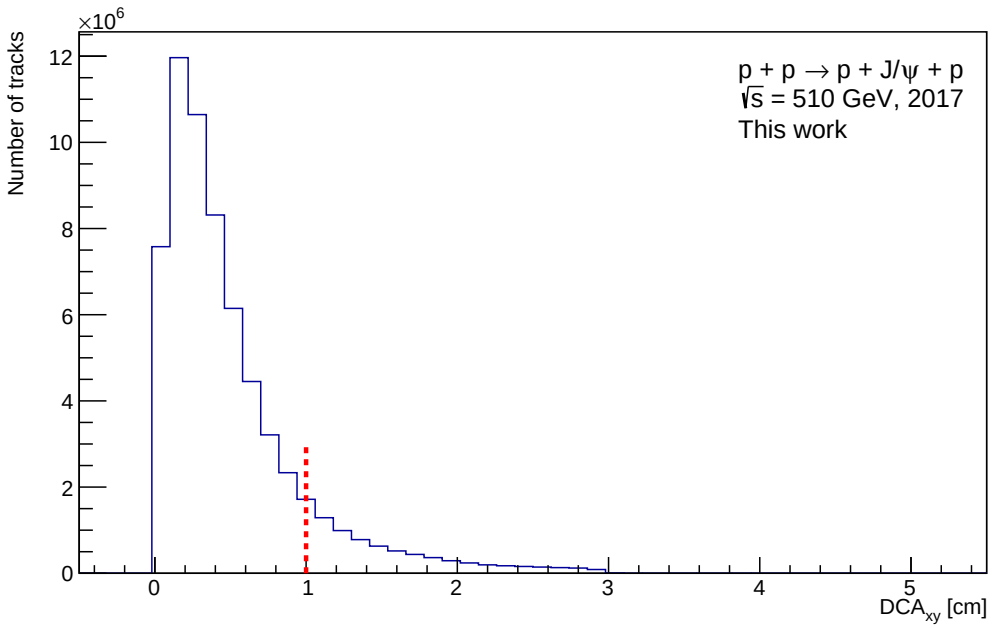

Figure 17: Histogram showing the DCA cut in xy plane. Red dashed line represents the limit value, where data below it are selected.

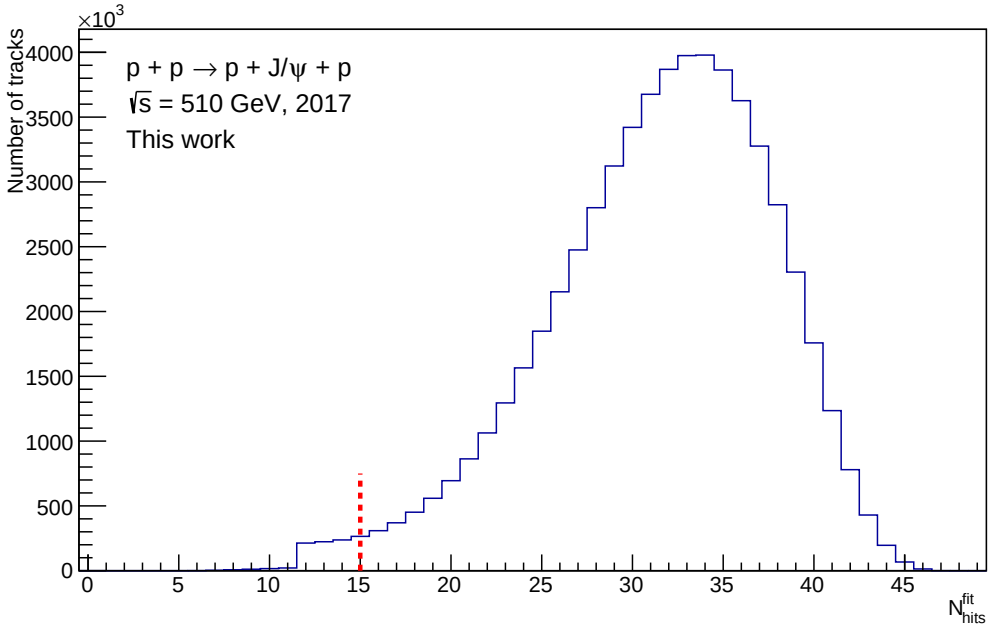

Figure 18: Histogram showing the $N_{\text{hits}}^{\text{fit}}$ cut. Red dashed line represents the limit value, where data above it are selected.

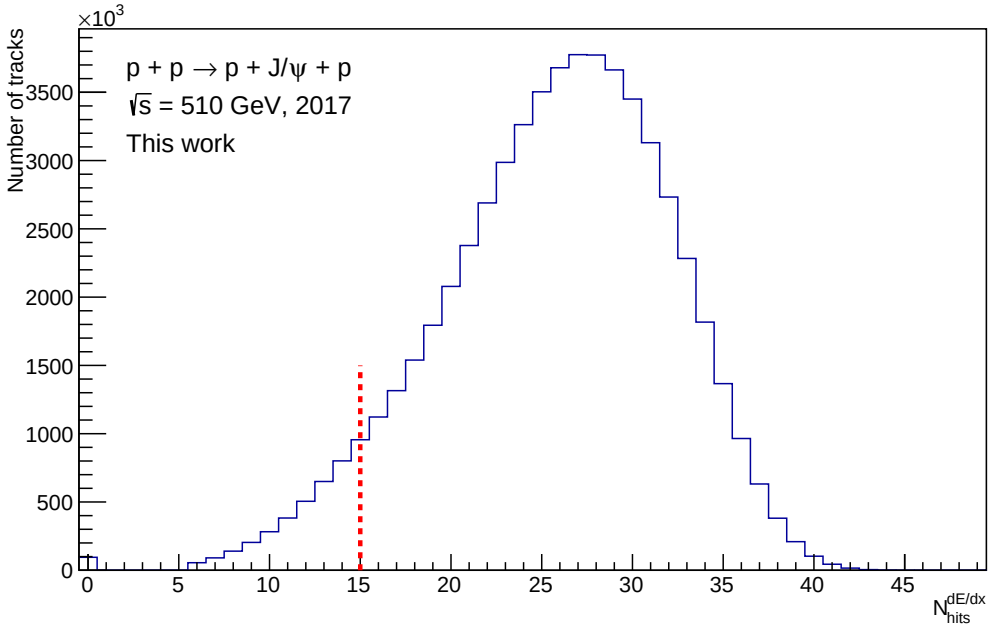

Figure 19: Histogram showing the $N_{\text{hits}}^{\mathrm{d}E/\mathrm{d}x}$ cut. Red dashed line represents the limit value, where data above it are selected.

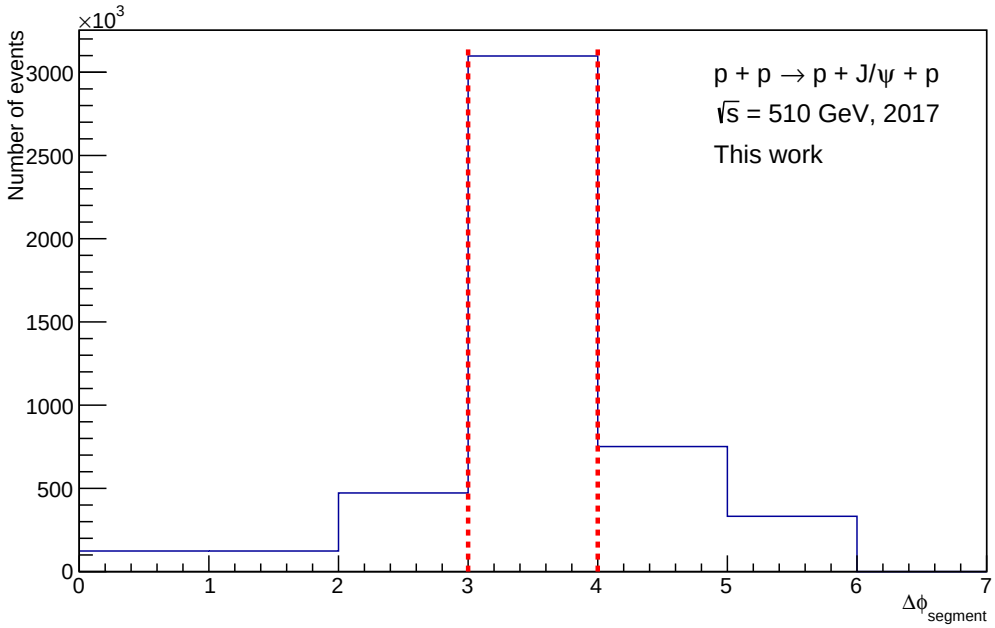

Figure 20: Histogram showing the back to back cut according to the BEMC segments. Red dashed lines represent the limit values used, where the selected events are in between.

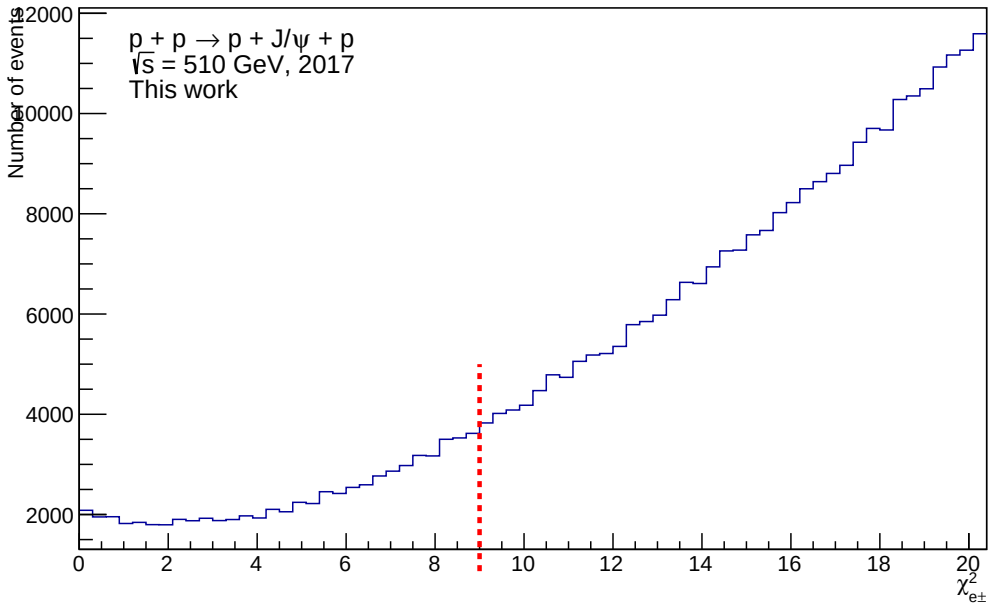

Figure 21: Histogram showing the χ^2 cut for electron and positron PID. Red dashed line represents the limit value, where data below it are selected.

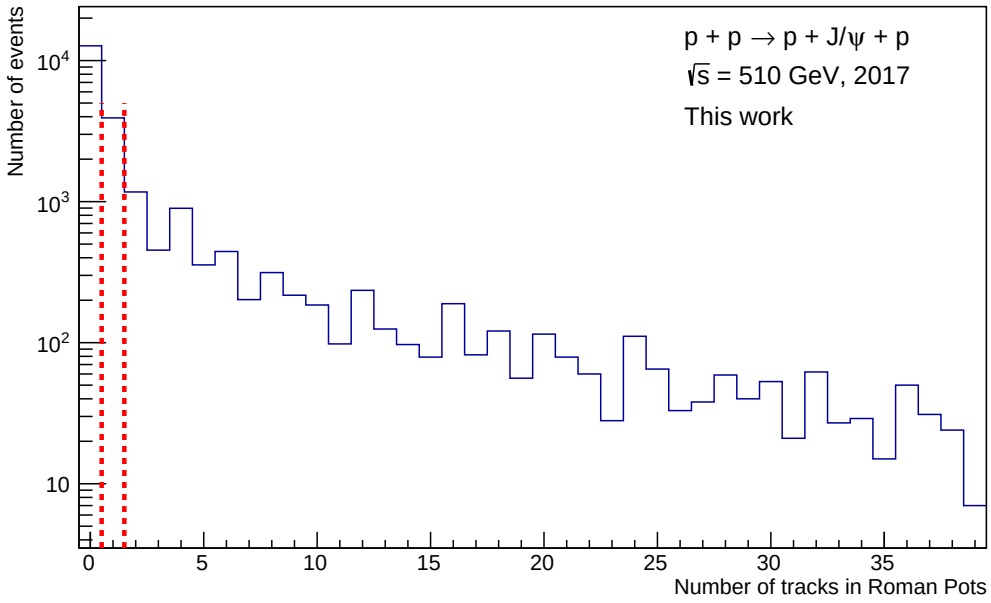

Figure 22: Histogram showing the cut on the number of RP tracks. Red dashed lines represent the limit values used, where the selected events are in between.

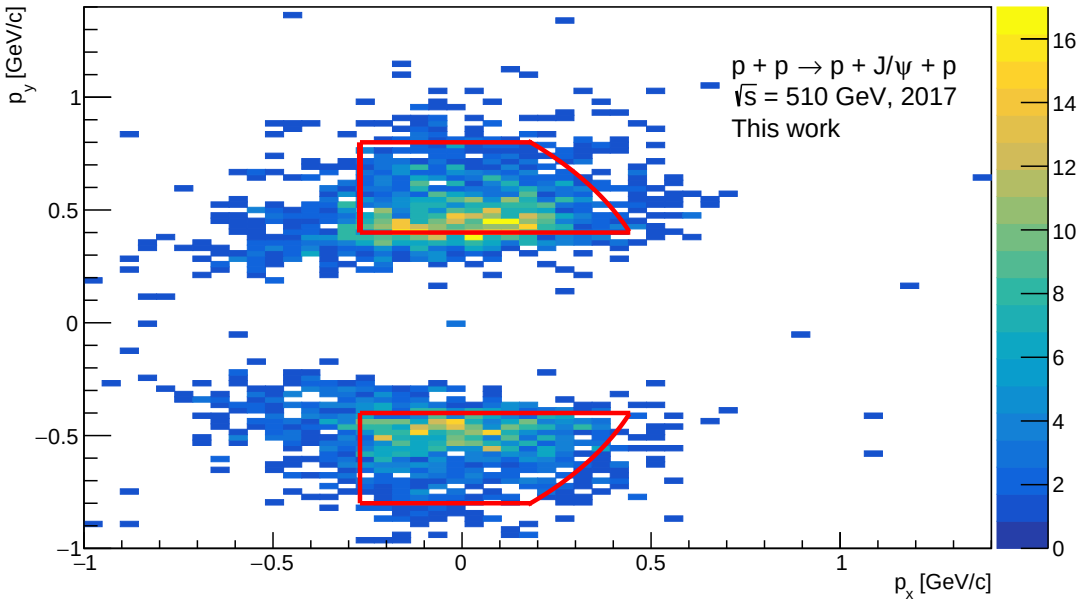

Figure 23: A 2D histogram showing the fiducial cut on RP track momentum. Red dashed lines represent the limit values used, where the selected events are bordered by them.